Nonlinear Evolution of Gravitational Fragmentation Regulated by Magnetic Fields and Ambipolar Diffusion

Shantanu Basu [a,*], Glenn E. Ciolek [b], and James Wurster [a]

[a] *Department of Physics and Astronomy, University of Western Ontario, London, Ontario N6A 3K7, Canada*

[b] *Department of Physics, Applied Physics, and Astronomy, Rensselaer Polytechnic Institute, 110 W. 8th Street, Troy, NY 12180, USA*

Abstract

We present results from an extensive set of simulations of gravitational fragmentation in the presence of magnetic fields and ambipolar diffusion. The thin-sheet approximation is employed, with an ambient magnetic field that is oriented perpendicular to the plane of the sheet. Nonlinear development of fragmentation instability leads to substantial irregular structure and distributions of fragment spacings, fragment masses, shapes, and velocity patterns in model clouds. We study the effect of dimensionless free parameters that characterize the initial mass-to-flux ratio, neutral-ion coupling, and external pressure associated with the sheet. The average fragmentation spacing in the nonlinear phase of evolution is in excellent agreement with the prediction of linear perturbation theory. Both significantly subcritical *and* highly supercritical clouds have average fragmentation scales $\langle \lambda \rangle \approx 2\pi Z_0$, where Z_0 is the initial half-thickness of the sheet. In contrast, the qualitatively unique transcritical modes can have $\langle \lambda \rangle$ that is at least several times larger. Conversely, fragmentation dominated by external pressure can yield dense cluster formation with much smaller values of $\langle \lambda \rangle$. The time scale for nonlinear growth and runaway collapse of the first core is ≈ 10 times the calculated growth time $\tau_{g,m}$ of the eigenmode with minimum growth time, when starting from a uniform background state with small-amplitude white-noise perturbations. Subcritical and transcritical models typically evolve on a significantly longer time scale than the supercritical models. Infall motions in the nonlinear fully-developed contracting cores are subsonic on the core scale in subcritical and transcritical clouds, but are somewhat supersonic in supercritical clouds. Core mass distributions are sharply peaked with a steep decline to large masses, consistent with the existence of a preferred mass scale for each unique set of dimensionless free parameters. However, a sum total of results for various initial mass-to-flux ratios yields a broad distribution reminiscent of observed core mass distributions. Core shapes are mostly near-circular in the plane of the sheet for subcritical clouds, but become progressively more elongated for clouds with increasing initial mass-to-flux ratio. Field lines above the cloud midplane remain closest to vertical in the ambipolar-drift driven core formation in subcritical clouds, and there is increasing amount of magnetic field curvature for clouds of increasing mass-to-flux ratio. Based on our results, we conclude that fragmentation spacings, magnitude of infall motions, core shapes, and, especially, the curvature of magnetic

field morphology, may serve as indirect observational means of determining a cloud's ambient mass-to-flux ratio.

1. Introduction

1.1. *Molecular Cloud Cores*

Star formation occurs in dense cores within interstellar molecular clouds. The existence and properties of dense cores are well established by studies of molecular spectral line emission (Myers & Benson, 1983; Benson & Myers, 1989; Jijina et al., 1999), submillimeter dust emission (Ward-Thompson et al., 1994; André et al., 1996; Kirk et al., 2005), and infrared absorption (Bacmann et al., 2000; Teixeira et al., 2005; Lada et al., 2007). The core formation process has been the subject of intense theoretical study for the past few decades. Ideas range from uninhibited gravitational fragmentation instability (Jeans, 1929; Larson, 1985, 2003), to ambipolar diffusion in a magnetically supported cloud (Mestel & Spitzer, 1956; Mouschovias, 1978; Shu et al., 1987), to a very rapid fragmentation due to pre-existing turbulent flows (Padoan et al., 1997; Klessen, 2001; Gammie et al., 2003). The last two ideas are related to scenarios for the nature of relatively low-density molecular cloud envelopes, which contain most of the mass of molecular clouds (see Goldsmith et al., 2008). In one scenario, they are magnetically-dominated and evolve due to ambipolar diffusion, a gravitationally-driven redistribution of mass amongst magnetic flux tubes (Mouschovias, 1978). The relatively low global star formation rate and efficiency in Galactic molecular clouds (see McKee, 1989) is used to argue that molecular cloud envelopes have a subcritical mass-to-flux ratio (see e.g. Shu et al., 1999; Elmegreen, 2007). Indirect empirical evidence based on the Chandrasekhar-Fermi (CF) method and velocity anisotropy measurements does imply that the low density ($n \sim 100$ cm^{-3}) regions are subcritical (Cortes et al., 2005; Heyer et al., 2008). The contrasting view is that the mass-to-flux ratio is supercritical on large scales, and that the star formation rate and efficiency are governed by supersonic turbulence (Mac Low & Klessen, 2004). This requires either a continual replenishment of rapidly dissipating turbulence, or a relatively rapid dispersal of the cloud envelopes. The focus of this paper is the fragmentation of embedded and relatively quiescent dense regions, and not on the nature of the larger envelopes. We study the effect of small-amplitude perturbations on a variety of cloud models with different mass-to-flux ratios, degrees of magnetic coupling, and external pressures.

For the purpose of this paper, we refer to any individual unit of star formation, which leads typically to a single or small multiple star system, as simply a "core". However, astronomers often subdivide this concept into two observational categories, that of "prestellar core" and "prestellar condensation". The former term is often used to describe the

---

* Corresponding author.

Email addresses: `basu@astro.uwo.ca` (Shantanu Basu), `cioleg@rpi.edu` (Glenn E. Ciolek).

extended (mean density $n \sim 10^5$ cm^{-3}, size $s \sim 0.1$ pc, spacing $\lambda \sim 0.25$ pc) objects in regions of distributed star formation like the Taurus molecular cloud, while the latter term typically describes the more compact ($n \gtrsim 10^6 - 10^7$ cm^{-3}, $s \sim 0.02 - 0.03$ pc, $\lambda \sim 0.03$ pc) objects that are located within cluster-forming cores in, for example, Ophiuchus, Serpens, Perseus, and Orion (see discussion in Ward-Thompson et al., 2007). Both the prestellar cores in e.g., Taurus, and the cluster-forming cores (which harbor multiple condensations) in the other clouds occupy only a very small fraction of the total volume and mass of their larger, more turbulent, molecular cloud complex (e.g., Johnstone et al., 2004; Goldsmith et al., 2008). A compendium of current data from spectral line emission, dust emission, and infrared absorption tends to show that cores exhibit central density concentration (Ward-Thompson et al., 1994; André et al., 1996) subsonic inward motions (Tafalla et al., 1998; Williams et al., 1999; Lee et al., 2001; Caselli et al., 2002) that often extend beyond the nominal core boundary, near-uniform gas temperatures (Benson & Myers, 1989), subsonic internal turbulence (Myers, 1983; Fuller & Myers, 1993; Goodman et al., 1998), and near-critical magnetic field strengths, when detected by the Zeeman effect (Crutcher, 1999; Bourke et al., 2001) or inferred by the CF method (Crutcher et al., 2004).

The measured subsonic infall motions constitute indirect evidence for a force that mediates gravity. The mediative force may be due to the magnetic field, whose strength in dense regions is very close to the critical value for collapse (Crutcher, 1999). If the fragmenting region has a subcritical mass-to-flux ratio, then the formation of cores will be regulated by ambipolar diffusion, i.e. neutral molecules diffusing past ions that are tied to magnetic fields, and will occur on a time scale that may significantly exceed the local dynamical time for typical ionization fractions. Conversely, if the dense gas is supercritical, then the fragmentation takes place on a dynamical time scale. Basu & Ciolek (2004, hereafter BC04) studied the nonlinear development of fragmentation instability in clouds that were initially either critical or decidedly supercritical. They found that supercritical fragmentation is characterized by somewhat supersonic motions on the core scale (~ 0.1 pc) while critical fragmentation is characterized by subsonic inward motions on those scales. The nonlinear fragmentation of decidedly subcritical clouds is also presented in this paper as part of a comprehensive parameter study of the effects of mass-to-flux ratio, initial ionization fraction, and external pressure. We believe that the three broad categories of subcritical, transcritical, and supercritical fragmentation should all occur in the interstellar medium, and even within separate regions of a single molecular cloud complex. Our results can help to distinguish which mode of fragmentation is occurring in a given observed region.

The linear theory of fragmentation of a partially ionized, magnetic thin sheet has been presented by Ciolek & Basu (2006, hereafter CB06). An important quantity is the dimensionless critical mass-to-flux ratio, $\mu = 2\pi G^{1/2}\sigma/B$, where σ is the column density of a sheet and B is the strength of the magnetic field that is oriented perpendicular to the plane of the sheet. In the limit of flux-freezing, fragmentation can occur only if $\mu > 1$, i.e. the sheet is supercritical. Conversely, gravitationally-driven fragmentation instability cannot occur at all if $\mu < 1$, i.e. the sheet is subcritical. CB06 show that the inclusion of ambipolar drift in such a model means that fragmentation can occur for *all mass-to-flux ratios*, but on widely varying time scales and length scales. A very important result of CB06 is their Fig. 2 (see also Fig. 1 in this paper), which demonstrates that transcritical ($\mu \approx 1$) fragmentation has a preferred scale that can be many times larger than $\lambda_{\mathrm{T,m}}$, the

3

wavelength of maximum growth rate in the thermal (i.e. nonmagnetic) limit. The latter is actually the preferred scale for both highly supercritical *and* highly subcritical clouds. This is because gravitational instability in subcritical clouds develops by ambipolar drift of neutrals past near-stationary magnetic field lines, and occurs on the ambipolar diffusion time scale rather than the dynamical time scale (see also Langer, 1978; Mouschovias, 1978). The "resonant" transcritical modes with preferred scale $\lambda_{g,m} \gg \lambda_{T,m}$ occur due to a combination of ambipolar drift and field-line dragging; the latter leads to magnetic restoring forces that can stabilize the perturbations unless they are of the required large size. The time scale for ambipolar-diffusion mediated gravitational instability is also presented extensively in CB06. They showed that highly supercritical clouds undergo gravitational instability on the dynamical time $t_d \approx Z/c_s$, where Z is the half-thickness (effectively the scale height) of the sheet and c_s is the isothermal sound speed. On the other hand, highly subcritical clouds undergo instability on the quasistatic ambipolar diffusion time $\tau_{AD} \approx 10\,Z/c_s$ for typical ionization fraction. Transcritical clouds undergo a hybrid instability on an intermediate time scale – see also Zweibel (1998) for a similar result. Also, we note that the inclusion of nonlinear fluctuations can reduce the ambipolar diffusion time under certain circumstances (Fatuzzo & Adams, 2002; Zweibel, 2002); we do not model such effects in this paper.

Our nonlinear simulations represent a significant extension of the parameter space of models from that presented by BC04. It similarly extends the parameter space studied by Indebetouw & Zweibel (2000), who presented nonaxisymmetric evolution of an infinitesimally thin subcritical sheet, including the effects of magnetic tension but ignoring magnetic pressure. Recent fully three-dimensional simulations by Kudoh et al. (2007), including magnetic fields and ambipolar diffusion, have confirmed the basic results of BC04. However, that paper presents three representative models, and an extensive parameter study remains computationally out of reach. Here, in addition to a parameter study, we carry out large numbers of simulations for *each* unique set of parameters. This is done in order to compile statistics on core spacings, mass distributions, and shapes. All simulations end at the time of the runaway central collapse of the first core, hence we are compiling information about the early phases of star formation in a molecular cloud. The subsequent history of the molecular cloud, after it has been stirred up by the initial star formation, remains to be determined. This paper represents the product of a total of over 700 separate simulations for models with 14 distinct sets of dimensionless parameters.

An alternate approach to modeling fragmentation is to input turbulence directly into the dense thin-sheet model (e.g., Li & Nakamura, 2004; Nakamura & Li, 2005), rather than relegating its presence to an unmodeled envelope. This results in highly supersonic motions within the dense sheet itself, and more rapid formation of cores than in our models. We do not pursue that approach in the present study but leave it open to future investigation.

1.2. *Relation to Global Cloud Structure*

Our simulations represent an intermediate approach between attempting a global model of large-scale molecular cloud structure and of modeling the interior collapse of individual cores. Large-scale models need to account for the overall structure and

4

self-gravity of molecular clouds and cannot be realistically studied using a periodic-box model. Truly global three-dimensional models are computationally expensive and still rarely attempted. Smoothed particle hydrodynamics (SPH) techniques have been used successfully to model entire cluster-forming regions (Bate et al., 2003; Bonnell et al., 2003), and can explain some important features of star formation like mass segregation, binary fraction, and the initial mass function. These models are not fully global in that they do not include the effect of the molecular cloud envelopes. They also do not include the effect of magnetic fields or feedback from outflows, so they cannot address the observed low global star formation efficiency (SFE), $1-5\%$ (Lada & Lada, 2003). However, the latest version of such models (Price & Bate, 2008) does include flux-frozen magnetic fields and yields somewhat lower SFE's than the non-magnetic models. Another three-dimensional approach which is fully global and based on finite-difference or SPH techniques is modeling the formation of a molecular cloud from large-scale supersonic gas flows and the early evolution of the cloud (Vázquez-Semadeni et al., 2006, 2007; Heitsch et al., 2008; Hennebelle et al., 2008). These models yield an initially flattened cloud whose subsequent evolution is affected by several instabilities (thermal instability, thin-shell instability, and Kelvin-Helmholtz instability). The overall structure evolves away from a sheet-like configuration, but individual segments may be treated as such. Of the above mentioned studies, only the work of Hennebelle et al. (2008) includes the effect of magnetic fields, which may work to suppress some of the instabilities. It is not clear whether this is an important factor in that model. However, the smaller-scale simulation of Nakamura & Li (2008) does show the formation of a sheet-like structure due to the presence of a dynamically important magnetic field. Amongst our models, the cases with high bounding pressure may be most appropriate for the scenario of cloud formation due to colliding flows. Our low external pressure models are more appropriate to the alternate scenario where the flows that form a molecular cloud are driven by gravity and/or channeled by a large scale magnetic field, e.g. by the magneto-Jeans instability (Kim et al., 2002) or the Parker instability (Parker, 1966).

Despite the various theoretical emphases on flattened structure, we note that observations of molecular clouds reveal complex morphologies with projected shapes that may not look like globally flattened structures. Molecular clouds have been described variously in the literature as stratified objects supported by internally generated turbulence (McKee, 1999), or as fractal objects (Elmegreen & Falgarone, 1996) in which the internal pressure is not as relevant. Our local sheet model may be applicable to the dense subregions of the clouds (where stars actually form in weak or rich clusters) in either scenario. As an example from the first scenario described above, one-dimensional global models (Kudoh & Basu, 2003, 2006; Folini et al., 2004) of molecular clouds reveal that internally-driven turbulence yields large-amplitude motions in lower-density envelopes, while retaining transonic motions in embedded dense regions; the fragmentation of the latter may be described by our models. From an observational point of view, we may apply our models to dense star forming regions such as L1495 and HCl 2 in the Taurus molecular cloud (see Goldsmith et al., 2008), the L1688 cluster-forming core in Ophiuchus (Motte et al., 1998), or better yet to the Pipe Nebula (Muench et al., 2007), which represents an even earlier stage of evolution, with a large number of relatively quiescent prestellar cores that are found in a dense elongated region (the "stem" of the Pipe). This region may represent the best available laboratory for the study of the early stage of star formation, before feedback from star formation has significantly modified a cloud's

5

internal sructure and motions. There is also evidence that the stem of the Pipe Nebula is flattened along the direction of the mean magnetic field (Alves & Franco, 2007). This property is similar to the better established result for the elongated structures in Taurus (Goodman et al., 1990; Goldsmith et al., 2008).

2. Physical Model

We consider the evolution of weakly ionized, magnetic interstellar molecular clouds. The clouds are isothermal, having a temperature T. As presented in CB06, we model a cloud as a planar sheet or layer of infinite extent in the x- and y- directions of a Cartesian coordinate system (x, y, z). At each time t the sheet has a local vertical half-thickness $Z(x, y, t)$. We take our model clouds to be *thin*: by this we mean that for any physical quantity $f(x, y, z, t)$ the condition $f/\nabla_p f \gg Z$ is always satisfied, where $\nabla_p \equiv \hat{\boldsymbol{x}} \partial/\partial x + \hat{\boldsymbol{y}} \partial/\partial y$ is the planar gradient operator. The magnetic field that threads a cloud has the form

$$
\boldsymbol{B}(x, y, z, t) = \begin{cases} B_{z,\mathrm{eq}}(x, y, t)\hat{\boldsymbol{z}} & \text{for } |z| \leq Z(x, y, t), \\ B_z(x, y, z, t)\hat{\boldsymbol{z}} \\ +B_x(x, y, z, t)\hat{\boldsymbol{x}} + B_y(x, y, z, t)\hat{\boldsymbol{y}} & \text{for } |z| > Z(x, y, t), \end{cases}
\tag{1}
$$

where $B_{z,\mathrm{eq}}$ is the vertical magnetic field strength in the equatorial plane. For $|z| \to \infty$, $\boldsymbol{B} \to B_{\mathrm{ref}}\hat{\boldsymbol{z}}$, where B_{ref} is a uniform, constant reference magnetic field very far away from the sheet. The magnetic field components above the sheet can be determined from $B_{z,\mathrm{eq}}(x, y)$ at any time using the divergence-free nature of the magnetic field and the current-free approximation above the sheet (see CB06 for details).

Some simplification is obtained by integrating the physical system of equations governing the evolution (conservation of mass and momentum, Maxwell's equations, etc.) of a model cloud along the vertical axis from $z = -Z(x, y)$ to $z = +Z(x, y)$. In doing so, a "one-zone approximation" is used, in which the density and the x- and y- components of the neutral and ion velocities, as well as the x- and y- components of the gravitational field, are taken to be independent of height within the sheet. The volume density is calculated from the vertical pressure balance equation

$$
\rho c_s^2 = \frac{\pi}{2} G \sigma_n^2 + P_{\mathrm{ext}} + \frac{B_x^2 + B_y^2}{8\pi},
\tag{2}
$$

where P_{ext} is the external pressure on the sheet and B_x and B_y represent the values at the top surface of the sheet, $z = +Z$. This simplification is commonly referred to as the "thin-sheet approximation"; the motivation for and the physical reasonability of it is discussed at length in Section 2 of CB06. It is the nonaxisymmetric extension of the axisymmetric thin-sheet models used to study ambipolar diffusion and gravitational collapse in magnetic interstellar clouds, as originally developed by Ciolek & Mouschovias (1993) and Basu & Mouschovias (1994).

6

2.1. Basic Equations

We solve normalized versions of the magnetic thin-sheet equations as justified in CB06. The unit of velocity is taken to be c_s, the column density unit is $\sigma_{n,0}$, and the unit of acceleration is $2\pi G \sigma_{n,0}$, equal to the magnitude of vertical acceleration above the sheet. Therefore, the time unit is $t_0 = c_s/2\pi G \sigma_{n,0}$, and the length unit is $L_0 = c_s^2/2\pi G \sigma_{n,0}$. From this system we can also construct a unit of magnetic field strength, $B_0 = 2\pi G^{1/2} \sigma_{n,0}$. The unit of mass is $M_0 = c_s^4/(4\pi^2 G^2 \sigma_{n,0})$. Here, $\sigma_{n,0}$ is the uniform neutral column density of the background state, and G is the gravitational constant. With these normalizations, the equations used to determine the evolution of a model cloud are

$$\frac{\partial \sigma_n}{\partial t} = -\nabla_p \cdot (\sigma_n \boldsymbol{v}_n), \tag{3}$$

$$\frac{\partial}{\partial t}(\sigma_n \boldsymbol{v}_n) = -\nabla_p \cdot (\sigma_n \boldsymbol{v}_n \boldsymbol{v}_n) + \boldsymbol{F}_T + \boldsymbol{F}_M + \sigma_n \boldsymbol{g}_p, \tag{4}$$

$$\frac{\partial B_{z,\text{eq}}}{\partial t} = -\nabla_p \cdot (B_{z,\text{eq}} \boldsymbol{v}_i), \tag{5}$$

$$\boldsymbol{F}_T = -C_{\text{eff}}^2 \nabla_p \sigma_n, \tag{6}$$

$$\boldsymbol{F}_M = B_{z,\text{eq}} (\boldsymbol{B}_p - Z \nabla_p B_{z,\text{eq}}) + \mathcal{O}(\nabla_p Z), \tag{7}$$

$$\boldsymbol{v}_i = \boldsymbol{v}_n + \frac{\tilde{\tau}_{ni,0}}{\sigma_n} \left(\frac{\rho_{n,0}}{\rho_n}\right)^{k_i} \boldsymbol{F}_M, \tag{8}$$

$$C_{\text{eff}}^2 = \sigma_n^2 \frac{(3\tilde{P}_{\text{ext}} + \sigma_n^2)}{(\tilde{P}_{\text{ext}} + \sigma_n^2)^2}, \tag{9}$$

$$\rho_n = \frac{1}{4}\left(\sigma_n^2 + \tilde{P}_{\text{ext}} + \boldsymbol{B}_p^2\right), \tag{10}$$

$$Z = \frac{\sigma_n}{2\rho_n}, \tag{11}$$

$$\boldsymbol{g}_p = -\nabla_p \psi, \tag{12}$$

$$\psi = \mathcal{F}^{-1}\left[-\mathcal{F}(\sigma_n)/k_z\right], \tag{13}$$

$$\boldsymbol{B}_p = -\nabla_p \Psi, \tag{14}$$

$$\Psi = \mathcal{F}^{-1}\left[\mathcal{F}(B_{z,\text{eq}} - B_{\text{ref}})/k_z\right]. \tag{15}$$

In the above equations, $\sigma_n(x,y) = \int_{-Z}^{+Z} \rho_n(x,y)\,dz$ is the column density of neutrals, $\boldsymbol{B}_p(x,y) = B_x(x,y)\hat{\boldsymbol{x}} + B_y(x,y)\hat{\boldsymbol{y}}$ is the planar magnetic field at the top surface of the sheet, $\boldsymbol{v}_n(x,y) = v_x(x,y)\hat{\boldsymbol{x}} + v_y(x,y)\hat{\boldsymbol{y}}$ is the velocity of the neutrals in the plane, $\boldsymbol{v}_i(x,y) = v_{i,x}(x,y)\hat{\boldsymbol{x}} + v_{i,y}(x,y)\hat{\boldsymbol{y}}$ is the corresponding velocity of the ions, and the normalized initial mass density (in units of $\sigma_{n,0}/L_0$) $\rho_{n,0} = \frac{1}{4}(1 + \tilde{P}_{\text{ext}})$, where $\tilde{P}_{\text{ext}}$ is defined below. The operator $\nabla_p = \hat{\boldsymbol{x}}\,\partial/\partial x + \hat{\boldsymbol{y}}\,\partial/\partial y$ is the gradient in the planar directions within the sheet. The quantities $\psi(x,y)$ and $\Psi(x,y)$ are the scalar gravitational and magnetic potentials, respectively, also in the plane of the sheet. The vertical wavenumber $k_z = (k_x^2 + k_y^2)^{1/2}$ is a function of wavenumbers k_x and k_y in the plane of the sheet, and the operators $\mathcal{F}$ and $\mathcal{F}^{-1}$ represent the forward and inverse Fourier transforms, respectively, which we calculate numerically using an FFT technique. Terms of order $\mathcal{O}(\nabla_p Z)$ in $\boldsymbol{F}_M$, the magnetic force per unit area, are not written down for the sake of brevity, but are

included in the numerical code; their exact form is given in Sections 2.2 and 2.3 of CB06. All terms proportional to $\nabla_p Z$ are generally very small.

We also note that the effect of nonzero $\nabla_p Z$ and external pressure P_{ext} is accounted for in the vertically-integrated thermal pressure force per unit area, $\boldsymbol{F}_{\text{T}}$, through the use of C_{eff}^2. This can be seen by noting that

$$\boldsymbol{F}_{\text{T}} = \int_{-Z}^{+Z} \nabla_p P \, dz = \nabla_p \int_{-Z}^{+Z} P \, dz - 2P_{\text{ext}}\nabla_p Z$$
$$= 2\,\nabla_p(PZ - P_{\text{ext}}Z) \ , \tag{16}$$

where P is the pressure inside the sheet. In the above expression, we have used $P = P_{\text{ext}}$ at the upper and lower surfaces of the sheet, and also that $\nabla_p(+Z) = -\nabla_p(-Z)$. Using the ideal gas equation for an isothermal gas, $P = \rho_{\text{n}} c_{\text{s}}^2$, the expression for half-thickness (Eq. [11]), and the normalized equation for vertical hydrostatic equilibrium (Eq. [10], where we ignore the relatively small term $\boldsymbol{B}_p^2$ for simplicity), it is straightforward to derive the normalized expression for C_{eff}^2 (Eq. [9]).

The above equations contain the following dimensionless free parameters: $\tilde{P}_{\text{ext}} \equiv 2P_{\text{ext}}/\pi G\sigma_{\text{n},0}^2$ is the ratio of the external pressure acting on the sheet to the vertical self-gravitational stress of the reference state. The dimensionless neutral-ion collision time of the reference state, $\tilde{\tau}_{\text{ni},0} \equiv \tau_{\text{ni},0}/t_0$, expresses the effect of ambipolar diffusion. In the limit $\tilde{\tau}_{\text{ni},0} \to \infty$ there is extremely poor neutral-ion collisional coupling, such that the ions and magnetic field have no effect on the neutrals. The opposite limit, $\tilde{\tau}_{\text{ni},0} = 0$, corresponds to the neutrals being perfectly coupled to the ions due to frequent collisions, i.e. flux freezing. The neutral-ion collision time of the reference state is

$$\tau_{\text{ni},0} = 1.4\frac{m_{\text{i}} + m_{\text{H}_2}}{m_{\text{i}}}\frac{1}{n_{\text{i},0}\langle\sigma w\rangle_{\text{iH}_2}} \ , \tag{17}$$

where m_{i} is the ion mass, which we take to be 25 a.m.u., the mass of the typical atomic (Na^+, Mg^+) and molecular (HCO^+) ion species in clouds, $n_{\text{i},0}$ is the ion number density of the reference state, and $\langle\sigma w\rangle_{\text{iH}_2}$ is the neutral-ion collision rate, equal to 1.69×10^{-9} cm^3 s^{-1} for H_2-HCO^+ collisions (McDaniel & Mason, 1973). The factor of 1.4 in Eq. (17) accounts for the fact that the effect of helium is neglected in calculating the slowing-down time of the neutrals by collisions with ions. The parameter k_{i} is the exponent in the power-law expression that is used to calculate the ion density n_{i} as a function of neutral density n_{n}, namely,

$$n_{\text{i}} = \mathcal{K}n_{\text{n}}^{k_{\text{i}}} \ , \tag{18}$$

where we adopt $k_{\text{i}} = 1/2$ and $\mathcal{K} (\simeq 10^{-5}\text{cm}^{-3/2})$ for all models in this study (e.g., Elmegreen, 1979; Umebayashi & Nakano, 1980), but keep in mind that calculation of the ion chemistry network makes k_{i} a function of n_{n} (Ciolek & Mouschovias, 1998). Finally, $\tilde{B}_{\text{ref}} = B_{\text{ref}}/B_0 = B_{\text{ref}}/2\pi G^{1/2}\sigma_{\text{n},0}$ is the dimensionless magnetic field strength of the reference state. For physical clarity, we use instead the dimensionless mass-to-flux ratio of the background reference state:

$$\mu_0 \equiv 2\pi G^{1/2}\frac{\sigma_{\text{n},0}}{B_{\text{ref}}} = \tilde{B}_{\text{ref}}^{-1} \ , \tag{19}$$

8

where $(2\pi G^{1/2})^{-1}$ is the critical mass-to-flux ratio for gravitational collapse in our adopted thin-sheet geometry (CB06). Models with $\mu_0 < 1$ ($\tilde{B}_{\rm ref} > 1$) are subcritical clouds, and those with $\mu_0 > 1$ ($\tilde{B}_{\rm ref} < 1$) are supercritical. The initial mass-to-flux ratio is also related to the commonly-used plasma parameter

$$\beta_0 \equiv \frac{\rho_{\rm n,0}\, c_{\rm s}^2}{(B_{\rm ref}^2/8\pi)} = \mu_0^2\,(1 + \tilde{P}_{\rm ext}). \tag{20}$$

Typical values of our units are

$$c_{\rm s} = 0.188 \left(\frac{T}{10\ {\rm K}}\right)^{1/2}\ {\rm km\ s^{-1}}, \tag{21}$$

$$t_0 = 3.65 \times 10^4 \left(\frac{T}{10\ {\rm K}}\right)^{1/2} \left(\frac{10^{22}\ {\rm cm^{-2}}}{N_{\rm n,0}}\right)\ {\rm yr}, \tag{22}$$

$$L_0 = 7.02 \times 10^{-3} \left(\frac{T}{10\ {\rm K}}\right) \left(\frac{10^{22}\ {\rm cm^{-2}}}{N_{\rm n,0}}\right)\ {\rm pc} \tag{23}$$

$$= 1.45 \times 10^3 \left(\frac{T}{10\ {\rm K}}\right) \left(\frac{10^{22}\ {\rm cm^{-2}}}{N_{\rm n,0}}\right)\ {\rm AU},$$

$$M_0 = 9.19 \times 10^{-3} \left(\frac{T}{10\ {\rm K}}\right)^2 \left(\frac{10^{22}\ {\rm cm^{-2}}}{N_{\rm n,0}}\right)\ M_\odot, \tag{24}$$

$$B_0 = 63.1 \left(\frac{N_{\rm n,0}}{10^{22}\ {\rm cm^{-2}}}\right)\ \mu{\rm G}. \tag{25}$$

Here, we have used $N_{\rm n,0} = \sigma_{\rm n,0}/m_{\rm n}$, where $m_{\rm n} = 2.33\,m_{\rm H}$ is the mean molecular mass of a neutral particle for an H_2 gas with a 10% He abundance by number. Furthermore, we may calculate the number density of the background state as

$$n_{\rm n,0} = 2.31 \times 10^5 \left(\frac{10\ {\rm K}}{T}\right) \left(\frac{N_{\rm n,0}}{10^{22}\ {\rm cm^{-2}}}\right)^2 \left(1 + \tilde{P}_{\rm ext}\right)\ {\rm cm^{-3}}. \tag{26}$$

The dimensional background reference magnetic field strength for a given model is simply $B_{\rm ref} = B_0/\mu_0$. Finally, the ionization fraction ($= n_{\rm i}/n_{\rm n}$) in the cloud may be expressed as

$$x_{\rm i} = \mathcal{K} n_{\rm n}^{-1/2} = 3.45 \times 10^{-8} \left(\frac{0.2}{\tilde{\tau}_{\rm ni,0}}\right) \left(\frac{10^5\ {\rm cm^{-3}}}{n_{\rm n}}\right)^{1/2} \left(1 + \tilde{P}_{\rm ext}\right)^{-1/2}. \tag{27}$$

2.2. *Numerical Techniques, Boundary and Initial Conditions*

The system of Eqs. (3) - (15) are solved numerically in (x, y) coordinates using a multifluid non-ideal MHD code that was specifically developed for this purpose (BC04; CB06). Partial derivatives $\partial/\partial x$ and $\partial/\partial y$ are replaced with their finite-difference equivalents. Gradients are approximated using three-point central differences between mesh cells, while advection of mass and magnetic flux is prescribed by using the monotonic upwind scheme of van Leer (1977). Evolution of a model is carried out within a square computational domain of size $L \times L$, spanning the region $-L/2 \leq x \leq L/2$ and $-L/2 \leq$

$y \leq L/2$. Typically, L is taken to be several times larger (up to a factor of 4) than the characteristic length scale of maximum gravitational instability $\lambda_{\rm g,m}$ (CB06; see, also, Section 3 below). The computational domain is then divided into a set of N^2 equally-sized mesh cells, each having an area $L/N \times L/N$. Most of our simulations are run with $L = 16\pi L_0$ and $N = 128$, and some have $L = 64\pi L_0$ and $N = 512$, so that the grid size $\Delta x = \Delta y = 0.393 L_0$ in all cases. The mass resolution is then $\Delta M = 0.154 M_0$, or $1.42 \times 10^{-3} M_\odot$ using the standard values in Eq. (24).

The numerical method of lines (Schiesser, 1991) is employed, i.e. the first-order partial differential equations (3) - (5) are converted into a set of coupled ordinary differential equations (ODE's) in time, with one ODE for each physical variable at each cell. Hence, the system of ODE's has the form $d\boldsymbol{\mathcal{Y}}/dt = \boldsymbol{\mathcal{G}}(\boldsymbol{\mathcal{Y}}, t)$, where $\boldsymbol{\mathcal{Y}}$ and $\boldsymbol{\mathcal{G}}$ are both arrays of size VN^2, V being the number of dependent variables. Time-integration of this system of ODE's is performed by using an Adams-Bashforth-Moulton predictor-corrector subroutine (Shampine, 1994). Numerical solution of Fourier transforms and inverse transforms, necessary to calculate the gravitational and magnetic potentials ψ and Ψ at each time step (see Eqs. [13] and [15]), is done by using fast Fourier transform techniques (Press et al., 1996).

Periodic conditions are applied to all physical variables at the boundary of the computational domain. The background reference state of a model cloud is characterized by a uniform column density $\sigma_{\rm n,0}$ and magnetic field $B_{z,\rm eq,0}\hat{\boldsymbol{z}} = B_{\rm ref}\hat{\boldsymbol{z}}$. This means that the gravitational and magnetic forces are each identically zero in the uniform background state. The evolution of a model cloud is started at time $t = 0$ by superposing a set of perturbations $\delta\sigma_{\rm n}(x, y)$ that are random white noise with a root-mean-squared (rms) value that is 3% of $\sigma_{\rm n,0}$. To preserve the same local mass-to-flux ratio $\sigma_{\rm n}/B_{z,\rm eq}$ as in the uniform background state, initial magnetic field perturbations $\delta B_{z,\rm eq} = (\delta\sigma_{\rm n}/\sigma_{\rm n,0})B_{\rm ref}$ are also introduced.

Detailed tests of the accuracy of this MHD code were described in CB06. Full code runs were compared to exact linear solutions for the gravitationally unstable modes of thin-sheet magnetic clouds. The code was found to be in excellent agreement with these solutions. It correctly captured the temporal evolution of a model cloud in the linear regime of collapse, as exemplified by the growth time of the gravitational instability $\tau_{\rm g}$ for a given fragmentation length scale λ, for various values of the initial parameters μ_0, $\tilde{\tau}_{\rm ni,0}$, and $\tilde{P}_{\rm ext}$. In addition, we have run flux-freezing tests of subcritical models with random perturbations and verified that no spurious gravitational instability occurs in the absence of ambipolar diffusion.

The principal motivation for our modeling clouds as thin sheets is that it significantly reduces the computational complexity of studying star formation, while still retaining many fundamental physical features necessary to understanding the dynamics of core formation and collapse within interstellar clouds. For instance, although model clouds are thin, they are not infinitesimally so, and we are able to incorporate both magnetic pressure and magnetic tension supporting forces (see Eq. [7]). Additionally, the vertical integration (along the direction of the z-axis) that is employed to derive the system of governing equations in the thin-sheet approximation (Eqs. [3] - [15]) has the effect of turning the fully three-dimensional gravitational collapse problem into a computationally more tractable two-dimensional problem. As a result of these computational savings, our numerical code is able to run efficiently on a single workstation with minimal cpu times. Depending on the initial parameters, a full simulation can be completed in as little as an

hour or at most a single day. Hence, we are able to quickly generate a large number of models covering the entire physically relevant range of our free parameters, and produce a large quantity of models that can be used for statistical analysis. By contrast, three-dimensional MHD models require a dedicated workstation or a computer cluster, and their simulation completion times are orders of magnitude greater than that needed for our thin-sheet models. Our new code is written in the IDL programming language, which significantly speeds up the processes of code development, debugging, and visualization.

We have also developed software to analyze the masses and shapes of cores arising from our simulations. In any snapshot of the evolution, we first isolate regions with column density (or mass-to-flux ratio in some cases) above some threshold value. Thresholds are usually chosen to be high enough that multiple peaks do not fall within a single contiguous region above the threshold. In cases where this happens, we have the option of manually isolating the cores. The mass of each core is found by adding the masses of each computational zone in the isolated region above the threshold. To determine the size and shape of a core we use the MPFITELLIPSE routine written in IDL by C. Markwardt, which returns the best-fit ellipse to the set of zones that constitute each core. The semimajor and semiminor axes of the best-fit ellipse, a and b, respectively, are obtained and used to determine the size $s = \sqrt{ab}$ and axis ratio b/a of each core. The vertical half-thicknesses Z of the zones within each core are averaged to find a mean half-thickness. The mean separation of fragments are found by locating, for each density peak associated with a core, the nearest peak of a neighboring core. These values are averaged over all cores in a simulation and over multiple model realizations. The periodic boundary conditions are also accounted for; we count any possible nearest neighbor that is just across the periodic boundary.

3. Results

3.1. *Overview*

The efficiency of our two-dimensional code allows us to run a large number of simulations, with various combinations of the important parameters μ_0, $\tilde{\tau}_{\mathrm{ni,0}}$, and $\tilde{P}_{\mathrm{ext}}$. For each unique set of parameters we are also able to run a multitude of independent model realizations. Each realization is distinct in specific details, since the evolution is initiated by random (white noise) small-amplitude perturbations. However, the independent realizations are statistically similar, and running a large number of models allows us to assess the level of randomness that contributes to distributions of various calculated quantities.

Table 1 contains the parameters for each of ten models as well as the predicted minimum growth time $\tau_{\mathrm{g,m}}$, the associated wavelength of maximum instability $\lambda_{\mathrm{g,m}}$, and the implied fragmentation mass $M_{\mathrm{g,m}} \equiv \pi \sigma_{\mathrm{n,0}} \lambda_{\mathrm{g,m}}^2 / 4$, all obtained from the linear perturbation analysis of CB06. The first two quantities are in normalized form, but the masses have been converted to $M_\odot$ using the standard values in Eq. (24). Some insight into the numerical values of $\tau_{\mathrm{g,m}}$ and $\lambda_{\mathrm{g,m}}$ in Table 1 can be obtained by considering the growth rate and fragmentation scale of the fastest growing mode in the limit of no magnetic field, but finite external pressure. From the results of CB06, we find

11

$$\tau_{\mathrm{g}}(\tilde{P}_{\mathrm{ext}}, \tilde{B}_{\mathrm{ref}} = 0) = 2\frac{(1 + 3\tilde{P}_{\mathrm{ext}})^{1/2}}{(1 + \tilde{P}_{\mathrm{ext}})}\frac{L_0}{c_{\mathrm{s}}} = (1 + 3\tilde{P}_{\mathrm{ext}})^{1/2}\frac{Z_0}{c_{\mathrm{s}}}, \tag{28}$$

$$\lambda_{\mathrm{g}}(\tilde{P}_{\mathrm{ext}}, \tilde{B}_{\mathrm{ref}} = 0) = 4\pi\frac{(1 + 3\tilde{P}_{\mathrm{ext}})}{(1 + \tilde{P}_{\mathrm{ext}})^2}L_0 = 2\pi\left(\frac{1 + 3\tilde{P}_{\mathrm{ext}}}{1 + \tilde{P}_{\mathrm{ext}}}\right)Z_0. \tag{29}$$

In the above equations, we have used the relation

$$Z_0 = \frac{2L_0}{(1 + \tilde{P}_{\mathrm{ext}})}. \tag{30}$$

These results show that in the limit $\tilde{P}_{\mathrm{ext}} \to 0$, the isothermal sheet has effective "Jeans length" $\lambda_{\mathrm{T,m}} = 4\pi L_0 = 2\pi Z_0$, and growth time $\tau_{\mathrm{T,m}} = 2L_0/c_{\mathrm{s}} = Z_0/c_{\mathrm{s}}$. The relation of these values to the sheet half-thickness and sound speed is intuitively understandable; the latter is essentially the dynamical time. The highly supercritical model 10, which also has low external pressure, does approach these limiting values of fragmentation scale and growth time. Equations (28)-(29) also bring out the interesting property that the fragmentation length and time scale of the isothermal sheet can be reduced significantly by increases in $\tilde{P}_{\mathrm{ext}}$, but that the fragmentation scale converges to a fixed multiple of Z_0 (i.e. $6\pi Z_0$) as $\tilde{P}_{\mathrm{ext}} \to \infty$. This property was first noted by Elmegreen & Elmegreen (1978) and studied further by Lubow & Pringle (1993). The significantly subcritical model 1 also has a fragmentation scale $\approx 2\pi Z_0$, since instability occurs via neutral drift past near-stationary field lines; however the growth time $\tau_{\mathrm{g,m}} \approx 10\,Z_0/c_{\mathrm{s}}$. The transcritical models 3 and 4 have values of $\tau_{\mathrm{g,m}}$ more similar to the subcritical models than the supercritical ones, although their fragmentation scales $\lambda_{\mathrm{g,m}}$ are large. Models 9 and 10 have have $\tilde{P}_{\mathrm{ext}} = 10$, resulting in much smaller values of $\tau_{\mathrm{g,m}}$ and $\lambda_{\mathrm{g,m}}$ than corresponding models with $\tilde{P}_{\mathrm{ext}} = 0.1$, although the dynamically important magnetic field raises the values of both above the nonmagnetic limits.

Our standard simulation box is four times larger in size than $\lambda_{\mathrm{T,m}}$ and more than twice $\lambda_{\mathrm{g,m}}$ for most models. Exceptions to this are model 4 and model 7, and these simulations are carried out in larger simulation boxes of quadruple size ($L = 64\,\pi L_0, N = 512$) when collecting information on core properties. The total mass in the simulation box with $L = 16\,\pi L_0 = 0.353\,(N_{\mathrm{n},0}/10^{22}\ \mathrm{cm}^{-2})^{-1}(T/10\ \mathrm{K})$ pc is $M = 2.53 \times 10^3\,M_0 = 23.2\,(N_{\mathrm{n},0}/10^{22}\ \mathrm{cm}^{-2})^{-1}(T/10\ \mathrm{K})^2\,M_\odot$. The expected fragmentation scales and masses for all models are significantly greater than the grid length resolution Δx and mass resolution ΔM quoted in Section 2.2.

Table 2 contains model parameters and key quantities at the end of each nonlinear model run. All runs end when $\sigma_{\mathrm{n,max}}/\sigma_{\mathrm{n},0} = 10$. This corresponds to a volume density enhancement $\rho_{\mathrm{n}}/\rho_{\mathrm{n},0} \approx 100$ for models with $\tilde{P}_{\mathrm{ext}} = 0.1$ and $\rho_{\mathrm{n}}/\rho_{\mathrm{n},0} \approx 10$ for models with $\tilde{P}_{\mathrm{ext}} = 10$. For each model, we list representative values of t_{run} [1], the physical time at which $\sigma_{\mathrm{n,max}} = 10\sigma_{\mathrm{n},0}$, $|v_{\mathrm{n}}|_{\mathrm{max}}$, the maximum neutral speed in the simulated region at that time, and $|v_{\mathrm{i}}|_{\mathrm{max}}$, the corresponding quantity for the ions. In general, models with relatively large values of $\mu_0, \tilde{\tau}_{\mathrm{ni},0}$, and $\tilde{P}_{\mathrm{ext}}$ tend to evolve faster than counterparts

---

[1] Experimentation with different rms amplitudes of the initial perturbation (so that $\delta\sigma_{\mathrm{n}}/\sigma_{\mathrm{n},0}$ is in the range 1%-6%), and variation of the power spectrum away from white noise but with the fixed standard rms value, reveal that the values of t_{run} can vary in the range 10%-20% from the values quoted in Table 2.

Table 1
Summary of Parameters and Results of Linear Theory

Model	μ_0	$\tilde{\tau}_{\mathrm{ni},0}$	$\tilde{P}_{\mathrm{ext}}$	$\tau_{\mathrm{g,m}}$	$\lambda_{\mathrm{g,m}}$	$M_{\mathrm{g,m}}$
1	0.5	0.2	0.1	20.2	14.3	1.48
2	0.8	0.2	0.1	17.6	16.5	1.96
3	1.0	0.2	0.1	14.3	24.3	4.26
4	1.1	0.2	0.1	10.8	54.9	21.8
5	2.0	0.2	0.1	3.21	23.9	4.12
6	10.0	0.2	0.1	2.11	13.9	1.40
7	1.0	0.1	0.1	27.5	28.5	5.86
8	1.0	0.4	0.1	7.93	20.0	2.89
9	0.5	0.2	10.0	4.87	3.43	0.09
10	1.0	0.2	10.0	3.33	4.99	0.18

Times and lengths are normalized to t_0 and L_0, respectively. Masses are converted to $M_\odot$ using Eq. (24).

with smaller values of these parameters. For the gravity-dominated models ($\tilde{P}_{\mathrm{ext}} = 0.1$), increasing values of μ_0 and/or $\tilde{\tau}_{\mathrm{ni},0}$ result in greater values of $|v_{\mathrm{n}}|_{\mathrm{max}}$. The values of $|v_{\mathrm{i}}|_{\mathrm{max}}$ illustrate that the systematic motions within the nonlinearly developed cores are gravitationally driven, so that ions lag behind neutrals somewhat. However, the difference between the speeds of the two species remains less than $0.1\,c_{\mathrm{s}}$. We perform an analysis of core properties as described in Section 2.2, after defining a core as an enclosed region with $\sigma_{\mathrm{n}}/\sigma_{\mathrm{n},0} \geq 2$ at the end of the simulation. Since each simulation typically yields only a handful of cores, the models are run a large number of times to generate significant core statistics. Models 1, 2, 3, and 5 were run 100 times each, while models 4 and 7, which need to be run on an expanded grid due to very large fragmentation scales, were run 22 and 6 times, respectively. Model 8 ran 50 times and models 9 and 10 were run 25 times each. Several averaged properties of the resulting cores are presented in columns 8-12 of Table 2. These quantities are $\langle\lambda\rangle$, the average distance between cores, $\langle M\rangle$, the average mass within a core (converted to $M_\odot$ using Eq. [24]), $\langle s\rangle$, the average size of a core, $\langle b/a\rangle$, the average axis ratio of a core, and $\langle Z\rangle$, the average value of the half-thickness of a core.

Fig. 1 shows the preferred fragmentation scales $\lambda_{\mathrm{g,m}}$ versus μ_0 from the linear analysis of CB06 for two separate values of the dimensionless external pressure ($\tilde{P}_{\mathrm{ext}} = 0.1$ on top and $\tilde{P}_{\mathrm{ext}} = 10$ below). Both lines represent models with $\tilde{\tau}_{\mathrm{ni},0} = 0.2$, which is our adopted standard value based on typical observationally-inferred ionization levels (see Eq. [27] above and Eq. [29] of CB06). Overlaid on each solid line are average core spacings $\langle\lambda\rangle$ (see Table 2) calculated from the nonlinear endpoint of our simulations. Each data point represents an average of core spacings for a large number (20 to 100) of simulations. The lower line contains $\langle\lambda\rangle$ data for up to 25 runs each of an additional four models with $\tilde{P}_{\mathrm{ext}} = 10$ that do not, for the sake of brevity, have their data compiled in Tables 1 and 2. *These results show that the linear theory can be used with confidence to predict the average fragmentation properties of clouds even in a fully nonlinear stage of development.* The tabulated fragmentation scales are slightly below the predictions of linear theory in the range $\mu_0 \approx 1 - 2$, for $\tilde{P}_{\mathrm{ext}} = 0.1$. This is due to occasional subfragmentation of the initially large (irregularly shaped) fragments as they become decidedly supercritical. We
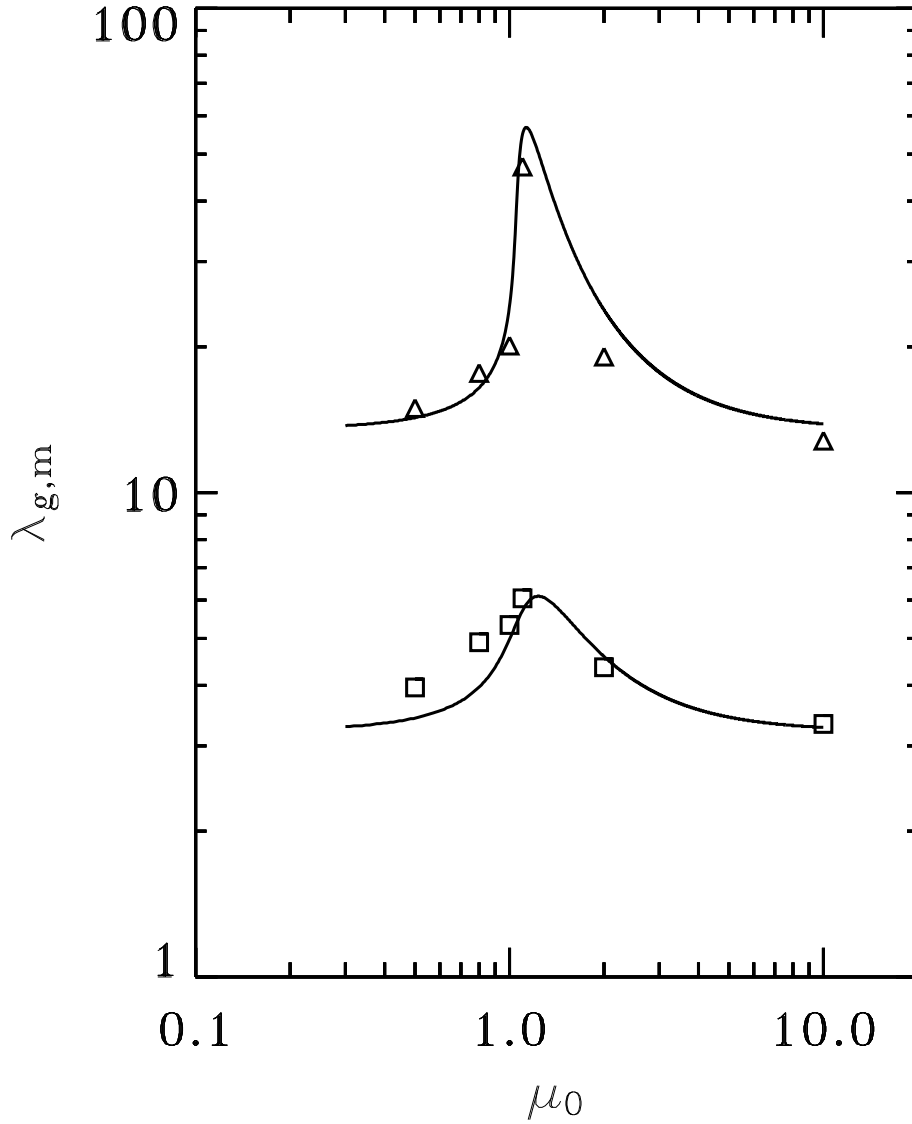
13

Fig. 1. Preferred fragmentation scales $\lambda_{\rm g,m}$ from linear stability analysis (Ciolek & Basu, 2006) compared with the average spacing of density peaks in the nonlinear simulations. The upper solid line is the calculated dependence of the wavelength with maximum growth rate $\lambda_{\rm g,m}$ versus μ_0 for fixed parameters $\tilde{\tau}_{\rm ni,0} = 0.2$ and $\tilde{P}_{\rm ext} = 0.1$. The lower solid line is the same but for $\tilde{P}_{\rm ext} = 10$. The triangles represent the average spacing of density peaks (with peak $\sigma_{\rm n} \geq 2\sigma_{\rm n,0}$) tabulated from a large number of simulations at each of $\mu_0 = 0.5, 0.8, 1.0, 1.1, 2.0$, and 10.0 with $\tilde{\tau}_{\rm ni,0} = 0.2$ and $\tilde{P}_{\rm ext} = 0.1$. The squares represent the same but with $\tilde{P}_{\rm ext} = 10$.

14

Table 2
Main Results for Model Clouds

Model	μ_0	$\tilde{\tau}_{\mathrm{ni},0}$	$\tilde{P}_{\mathrm{ext}}$	t_{run}	$|v_{\mathrm{n}}|_{\mathrm{max}}$	$|v_{\mathrm{i}}|_{\mathrm{max}}$	$\langle\lambda\rangle$	$\langle M\rangle$	$\langle s\rangle$	$\langle b/a\rangle$	$\langle Z\rangle$
1	0.5	0.2	0.1	204	0.39	0.35	15.0	1.26	1.25	0.74	0.71
2	0.8	0.2	0.1	167	0.62	0.55	17.7	1.56	1.49	0.81	0.72
3	1.0	0.2	0.1	121	0.70	0.64	20.1	3.26	2.09	0.69	0.65
4	1.1	0.2	0.1	88	0.95	0.90	47.1	6.62	3.23	0.66	0.75
5	2.0	0.2	0.1	23	1.1	1.0	19.1	3.41	2.08	0.57	0.67
6	10.0	0.2	0.1	12	1.2	1.2	12.8	0.99	1.04	0.53	0.70
7	1.0	0.1	0.1	261	0.66	0.62	31.4	3.29	2.13	0.77	0.78
8	1.0	0.4	0.1	61	0.73	0.63	18.5	2.02	1.69	0.67	0.71
9	0.5	0.2	10.0	44	0.70	0.63	4.0	0.34	0.60	0.62	0.072
10	1.0	0.2	10.0	22	0.50	0.38	5.3	0.46	0.74	0.60	0.074

Times and lengths are normalized to t_0 and L_0, respectively. Speeds are normalized to c_{s}. Masses are converted to $M_\odot$ using Eq. (24). Core data for models 4 and 7 are compiled from runs with $N = 512, L = 64\pi L_0$.

return to this issue when discussing the models with $\mu_0 = 1.1$.

3.2. The Effect of Varying μ_0

3.2.1. Time Evolution

Fig. 2 shows the time evolution of the maximum neutral column density $\sigma_{\mathrm{n,max}}$ and maximum mass-to-flux ratio μ_{max}, both normalized to their initial values, for models 1, 3, and 5, which have $\mu_0 = 0.5, 1.0$, and 2.0, respectively, and fixed parameters $\tilde{\tau}_{\mathrm{ni},0} = 0.2$ and $\tilde{P}_{\mathrm{ext}} = 0.1$. These three models have $\tau_{\mathrm{g,m}}/t_0 = 20.2, 14.3$, and 3.2, respectively. The actual time t_{run} to runaway collapse of a core, starting from small-amplitude white-noise perturbations, is about $7 - 10$ times $\tau_{\mathrm{g,m}}$ for these models. Review of Table 1 and Table 2 shows that $t_{\mathrm{run}}/\tau_{\mathrm{g,m}} \approx 7 - 10$ is a generic feature of all our models. The clouds with initial critical and subcritical mass-to-flux ratio have a prolonged period of dormancy, compared to the supercritical models. This is due to the need for ambipolar diffusion to operate before collapse sets in for both cases. The dashed lines in Fig. 2 show how much the mass-to-flux ratio changes during the evolution. The initially subcritical cloud requires a significant increase of μ_{max} before collapse begins. Although μ_{max} appears to be diverging at the end of the simulations, it is in fact increasing much more slowly than $\sigma_{\mathrm{n,max}}$, and will not asymptotically diverge. This can be seen in previously published work, i.e. in Fig. 2 of each of Ciolek & Mouschovias (1994) and Basu & Mouschovias (1994).

3.2.2. Column Density and Velocity Structure

Fig. 3 shows the column density map and velocity vectors of neutrals at the end of the simulations for parameters $\mu_0 = 0.5, 0.8, 1.0, 1.1, 2.0$, and 10.0, with $\tilde{\tau}_{\mathrm{ni},0} = 0.2$ and $\tilde{P}_{\mathrm{ext}} = 0.1$. All simulations end when $\sigma_{\mathrm{n,max}}/\sigma_{\mathrm{n},0} = 10$, but the time at which this is reached is different in each model. These times for the various models (in order of increas-
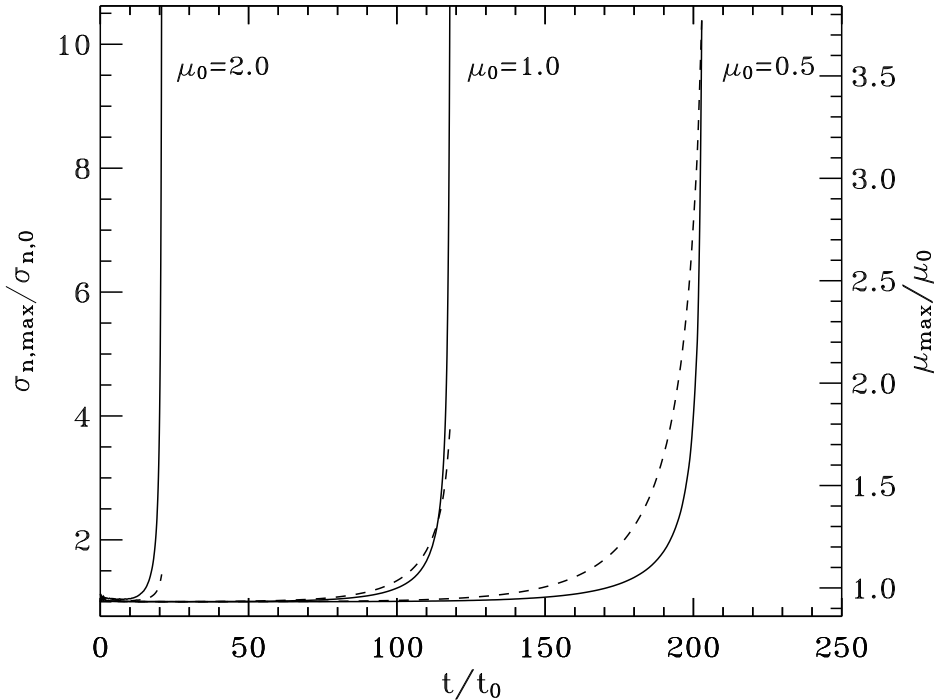
15

Fig. 2. Time evolution of maximum values of surface density and mass-to-flux ratio in three simulations. The solid lines show the evolution of the maximum value of surface density in the simulation, $\sigma_{n,max}/\sigma_{n,0}$, versus time t/t_0. This is shown for models 1, 3, and 5, which have initial mass-to-flux ratio values $\mu_0 = 0.5, 1$, and 2, respectively. For each model, a dashed line shows the evolution of the maximum mass-to-flux ratio in the simulation, μ_{max}, normalized to μ_0.

ing μ_0) are $t/t_0 = 203.7, 166.5, 120.9, 88.1, 22.8,$ and 12.4. There is a striking variation in the spacings of cores as μ_0 changes. The highly subcritical case $\mu_0 = 0.5$ fragments on essentially the nonmagnetic preferred scale $\lambda_{T,m} = 4\pi L_0$, since the evolution is charac- terized by diffusion of neutrals past near-stationary magnetic field lines, i.e. a Jeans-like instability but on a diffusive time scale. As predicted by the linear theory (CB06), there is a peak in the fragmentation spacing near $\mu_0 = 1$. The peak occurs at $\mu_0 = 1.1$ when $\tilde{\tau}_{ni,0} = 0.2$ and $\tilde{P}_{ext} = 0.1$. The predicted fragmentation scale is $\lambda_{g,m} = 4.2\,\lambda_{T,m}$, and indeed our simulation with box width $4\,\lambda_{T,m}$ yields only one core, although it seems to be undergoing a secondary fragmentation into two pieces.

The velocity vectors of the neutral flow are normalized to the same scale in each frame, and the horizontal or vertical spacing of the footpoints is equal to $0.5\,c_s$. There is a monotonic increase of the typical neutral speeds as μ_0 increases (see values of $|v_n|_{max}$ in Table 2). The supercritical models, unlike their subcritical and critical counterparts, have large-scale flow patterns with velocities in the approximate range $(0.5 - 1.0)\,c_s$, and maximum speeds associated with the most fully developed cores that are mildly supersonic at distances ~ 0.1 pc from the core centers. Interestingly, the essentially hydrodynamic model with $\mu_0 = 10$ has only somewhat greater systematic speeds than

16

the model with $\mu_0 = 2$. This is because the fragmentation scale is smaller, so that each core has a weaker gravitational influence on its surroundings at this stage of development. However, recall that the frames are at different physical times since the models with smaller values of μ_0 reach $\sigma_{n,max}/\sigma_{n,0} = 10$ at progressively later times. Spatial profiles of $\boldsymbol{v}_n$ in the vicinity of cores are presented in BC04, for some models, and we do not present them again in this paper. The trend of values of maximum neutral speed $|v_n|_{max}$ and maximum ion speed $|v_i|_{max}$ (Table 2) reveal the predictions of our models for the observable motions on the core scale. The infall motions are gravitationally driven, so that the ion speed lags the neutral speed in all cases. The overall rms speed in the entire simulation region is always quite small for both neutrals and ions. The rms speed of neutrals, $v_{n,rms}$, falls in the range $(0.05 - 0.21)\,c_s$ for the various models, and the corresponding quantity $v_{i,rms}$ in the range $(0.04 - 0.20)\,c_s$.

Since the standard box size $L = 16\,\pi L_0$ allows only one fragment to form initially in the model with $\mu_0 = 1.1$ (as seen in Fig. 3), we ran another model with four times larger box size but the same resolution, so that $L = 64\,\pi L_0$ and $N = 512$. This allows the formation of multiple fragments, since the preferred fragmentation scale from the linear theory is $\lambda_{g,m} = 54.9 L_0$. Fig. 4 shows the column density and velocity vectors at the end of one such simulation. Velocity vectors are again normalized such that the horizontal or vertical spacing between footpoints equals $0.5\,c_s$. This larger simulation does show that multiple fragments form with spacings approximately as predicted by the linear theory, but that there is also a tendency for cores to subfragment into two density peaks. An analysis of the result of 25 separate simulations with different random realizations of the initial state reveals that the average distance between density peaks is $47.1 L_0$, which is somewhat smaller than $\lambda_{g,m} = 54.9 L_0$. This is explained by the occasional presence of secondary density peaks within the initially formed fragments. While most model clouds undergo *single-stage fragmentation* into essentially thermal critical (Jeans-like) fragments of size $\approx \lambda_{T,m}$, the transcritical clouds form first-stage fragments many times larger than $\lambda_{T,m}$, followed by a possible *second-stage fragmentation* when the mass-to-flux ratio of the fragment becomes decidedly supercritical due to ambipolar diffusion. This second-stage fragmentation may be favored because both the preferred fragmentation scale and growth time of gravitational instability drop precipitously as a cloud makes the transition from transcritical to supercritical (see Figs. 1d and 2 of CB06). The initially rather large fragment may itself be prone to fragmentation because of its irregular shape.

Fig. 5 shows an alternate view of the column density, using surface plots at the end of simulation runs, with parameters corresponding to those of models 1, 3 and 5. These models start from different realizations of the initial state than those of the models presented in Fig. 3. Density peaks occur in different locations but represent an equivalent outcome statistically. Animations of the time evolution of the surface plots are available online [2] .

---

[2] The animations of the models shown in Figs. 5 and 6 reveal that they reach the final state with $\sigma_n/\sigma_{n,0} = 10$ in a time 15-20% less than that quoted in Table 2. This is because the initial perturbation is white noise but with the smallest wavelengths ($\lambda \leq 4$ grid cells) damped out. This results in slightly more power in the longer wavelengths (for a fixed rms perturbation level), including the preferred fragmentation scale $\lambda_{g,m}$, and a consequent quicker development of the favored mode.
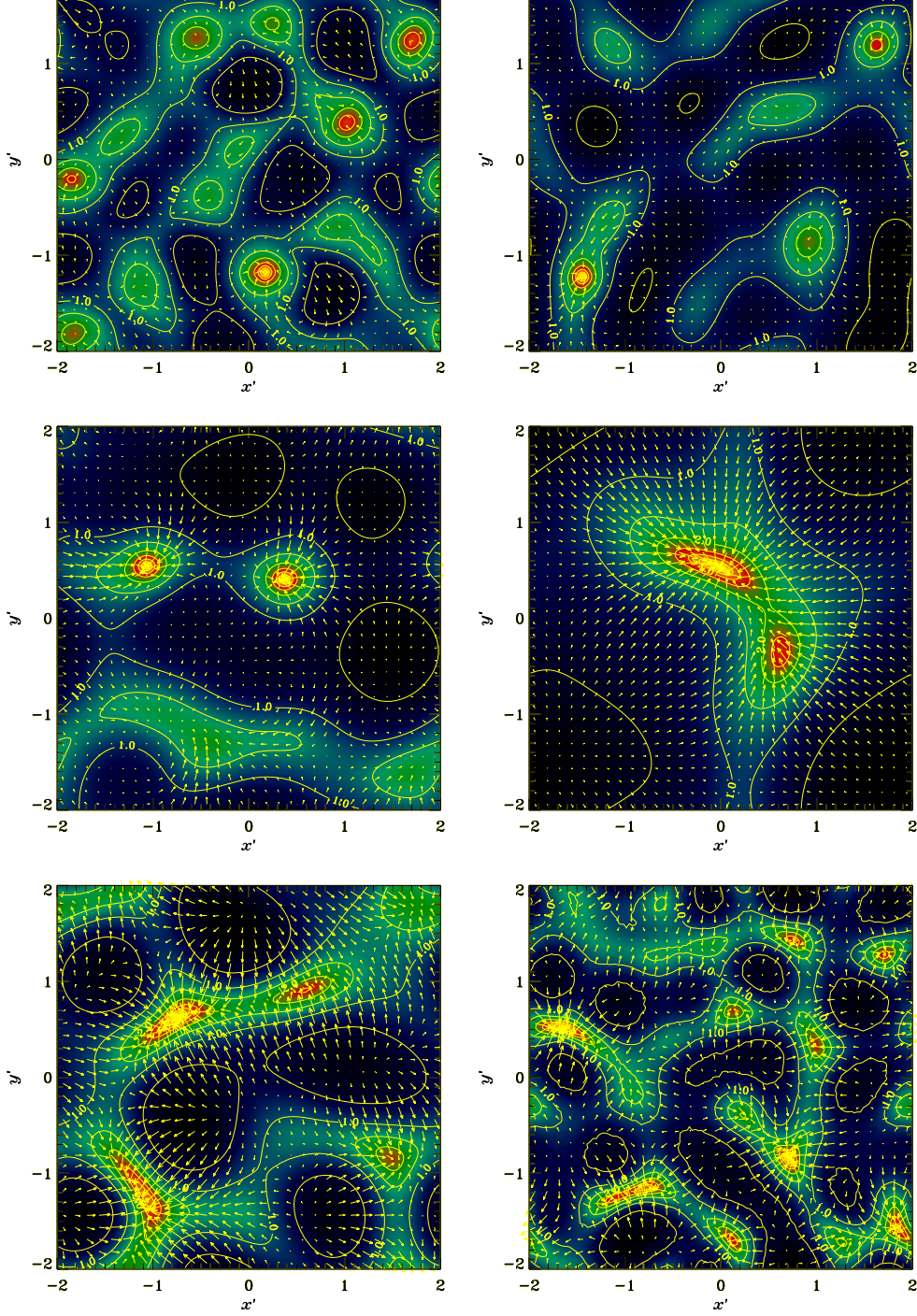
Fig. 3. Image and contours of column density $\sigma_n(x, y)/\sigma_{n,0}$, and velocity vectors of neutrals, for six different models at the time that $\sigma_{n,max}/\sigma_{n,0} = 10$. All models have $\tilde{\tau}_{ni,0} = 0.2$ and $\tilde{P}_{ext} = 0.1$. Top left: $\mu_0 = 0.5$. Top right: $\mu_0 = 0.8$. Middle left: $\mu_0 = 1.0$. Middle right: $\mu_0 = 1.1$. Bottom left: $\mu_0 = 2.0$. Bottom right: $\mu_0 = 10.0$. The color table is applied to the logarithm of column density and the contour lines represent values of $\sigma_n/\sigma_{n,0}$ spaced in multiplicative increments of $2^{1/2}$, having the values $[0.7,1.0,1.4,2,2.8,4.0,...]$. The horizontal or vertical distance between footpoints of velocity vectors corresponds to a speed $0.5\,c_s$. We use the normalized spatial coordinates $x' = x/\lambda_{T,m}$ and $y' = y/\lambda_{T,m}$, where $\lambda_{T,m}$ is the wavelength of maximum growth rate in the nonmagnetic limit with $P_{ext} = 0$.

18
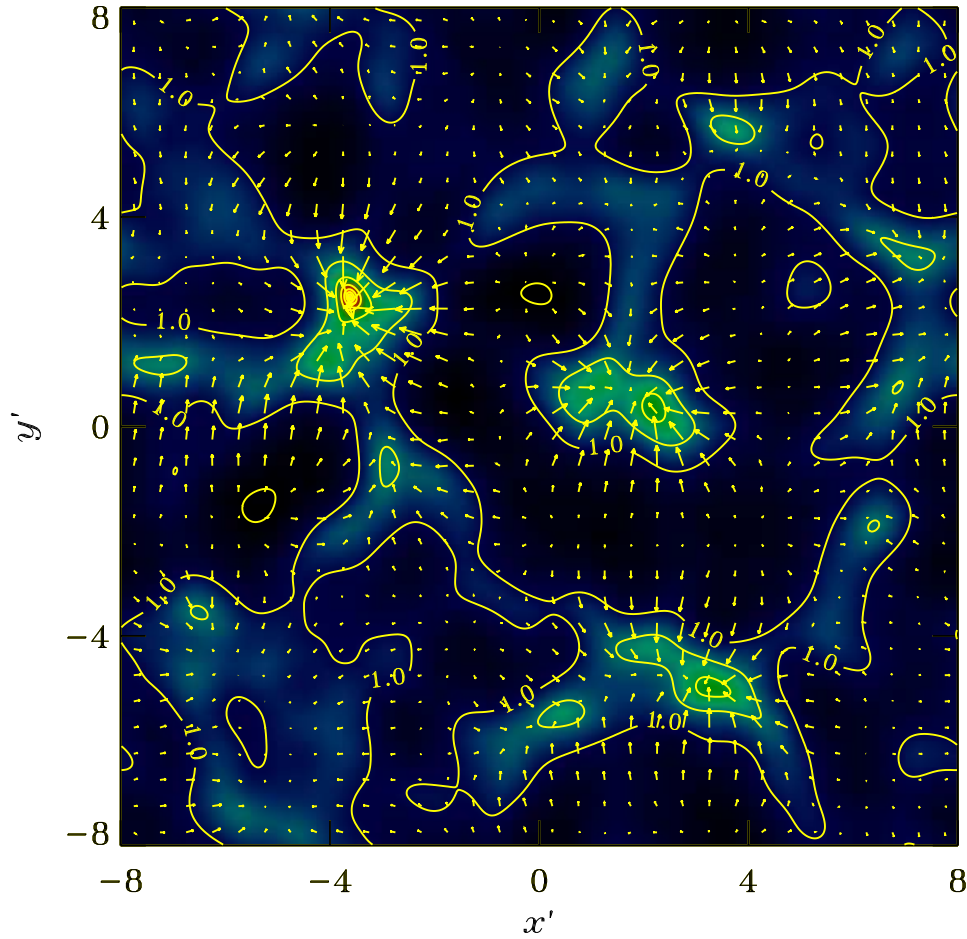
Fig. 4. Column density and velocity vectors as in Fig. 3 but with model 4 parameters ($\mu_0 = 1.1$) that is run with four times larger computational region in each direction. The simulation region consists of 512×512 zones. The horizontal or vertical distance between footpoints of velocity vectors corresponds to a speed $0.5\,c_{\rm s}$.
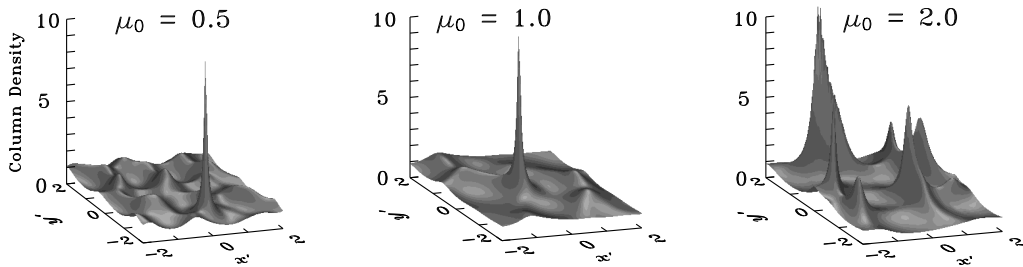
Fig. 5. Surface plot of column density $\sigma_{\rm n}(x,y)/\sigma_{\rm n,0}$ at the end of the simulation for models 1, 3, and 5 with (left to right) $\mu_0 = 0.5, 1.0, 2.0$. Animations of the time evolution for each model are available online.

19

3.2.3. *Magnetic Field Lines*

For the force-free and current-free region above our model sheet, the three-dimensional structure of the magnetic field is obtained by solving Laplace's equation for the scalar magnetic potential $\Psi_M(x, y, z)$. The two-dimensional Fourier Transform of the magnetic potential at any height z above the sheet is related to its known planar value $\Psi(x, y) = \Psi_M(x, y, z = 0)$ via

$$\Psi_M(x, y, z) = \mathcal{F}^{-1} \left\{ \mathcal{F}[\Psi(x, y)] \exp(-k_z |z|) \right\}. \tag{31}$$

In the above expression, $\mathcal{F}$ ($\mathcal{F}^{-1}$) represents the forward (inverse) Fourier Transform in a two dimensional (x, y) plane for a fixed z, Ψ is obtained from Eq. (15), and $k_z = (k_x^2 + k_y^2)^{1/2}$. We use the FFT technique to efficiently calculate Ψ_M at any height z, which then leads to the various components of the magnetic field above the sheet via $\boldsymbol{B} - B_{\mathrm{ref}}\hat{\boldsymbol{z}} = -\nabla\Psi_M$ (see CB06 for a justification of this expression).

Fig. 6 shows images of the final state column density for two models with $\mu_0 = 1.0$ and 2.0, respectively. These are also independent realizations and differ in specific details from models presented earlier. Overlaid on the column density images are the magnetic field lines extending above the sheet. These are three-dimensional images of a sheet plus field lines above, viewed from an angle of approximately $10°$ from the direction of the background magnetic field. Clearly, the supercritical model has more curvature in the field lines, as the contraction proceeds primarily with field-line dragging. The critical model produces its cores via a hybrid mode including both neutral-ion slip (ambipolar diffusion) and field-line dragging, hence the the lesser amount of field line curvature. The relative amounts of field line curvature in the cloud and within dense cores are quantified by calculating the quantity $\theta = \tan^{-1}(|B_p|/B_{z,\mathrm{eq}})$, where $|B_p| = (B_x^2 + B_y^2)^{1/2}$ is the magnitude of the planar magnetic field at any location on the sheet-like cloud. Hence, θ is the angle that a field line makes with the vertical direction at any location at the top or bottom surface of the sheet. To quantify the differences in field line bending from subcritical to transcritical to supercritical clouds, we note that models 1, 3, and 5, with $\mu_0 = (0.5, 1.0, 2.0)$, have average values $\theta_{\mathrm{av}} = (1.7°, 8.3°, 18°)$, and maximum values (probing the most evolved core in each simulation) $\theta_{\mathrm{max}} = (20°, 30°, 46°)$. For the model with $\mu_0 = 0.5$, θ_{max} is comparable to that presented in Fig. 2 of Ciolek (1996).

Our ability to model fragmentation with varying levels of magnetic support and neutral-ion slip opens up the possibility of making a detailed comparison of observed hourglass morphologies of magnetic field lines, where measured (e.g. Schleuning, 1998), with theoretical models so that the curvature of field lines may be used as a proxy to measure the ambient magnetic field strength.

3.2.4. *Shapes*

The core identification techniques described in Section 2.2 yield core sizes, shapes, and masses, whose average values are tabulated in Table 2. Here in Fig. 7 we present a more detailed histogram of core shape distributions for each of models 1 through 6. This isolates the effect of mass-to-flux ratio on core shapes. The statistics are generated by running each of model 1-3 and 5-6 for 100 distinct realizations with the usual box size ($L = 16\,\pi L_0, N = 128$). Model 4 is run 22 times due to the larger box size ($L = 64\,\pi L_0, N = 512$) necessitated by the large fragmentation scale. The number of cores generated are 547, 367, 187, 126, 272, and 659, for models 1 through 6, respectively. The
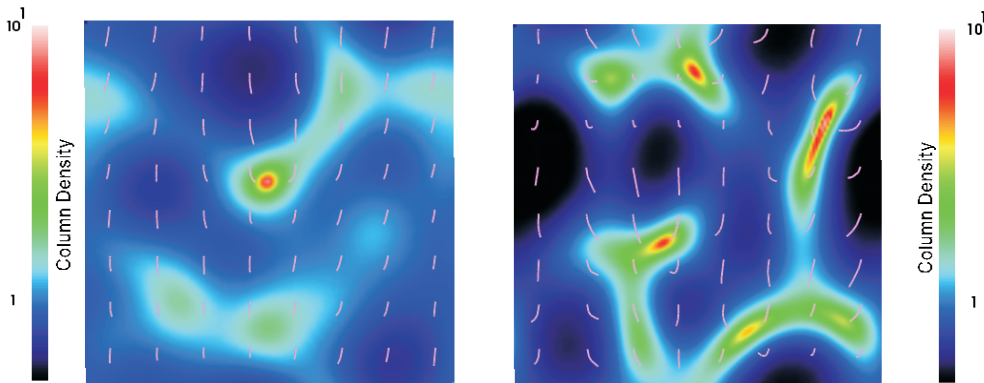
Fig. 6. Image of gas column density $\sigma_n(x, y)/\sigma_{n,0}$ and superposed magnetic field lines for models 3 and 5, with $\mu_0 = 1.0$ (left) and $\mu_0 = 2.0$ (right). The magnetic field lines extend above the sheet, and the image and field lines are seen from a viewing angle of about $10°$. Animations of the evolution of the column density are available online. The field lines appear in the last frame of the animation.

different numbers reflect the varying numbers of cores arising for each set of parameters (see Fig. 3) as well as the smaller number of runs for model 4. However, in each case we have sufficient numbers to make inferences about the differences between models.

Fig. 7 reveals in detail what is apparent by a visual inspection of Fig. 3. The core shape distribution contains many circular objects (axis ratio $b/a \approx 1$) for subcritical clouds, but contains progressively more elongated cores as μ_0 increases. All initially supercritical models have a peak axis ratio that is distinctly non-circular. All objects are also flattened in the vertical direction and usually have the shortest dimension along the magnetic field (see values of $\langle Z \rangle$ in Table 2). The underlying physical explanation is that quasistatic formation of cores (for $\mu_0 \leq 1$) allows for growth in all directions more equally, whereas dynamical gravity-dominated formation will strongly accentuate the anisotropies ($k_x \neq k_y$) that are present at the outset (see Miyama et al., 1987a,b).

The supercritical models have a mean axis ratio in the sheet plane ≈ 0.5, which is in rough agreement with the observed mean *projected* axis ratio of dense cores (Myers et al., 1991). However, a deprojection of the observed axis ratios yields intrinsic three-dimensional shapes that are inherently triaxial (Jones et al., 2001; Jones & Basu, 2002; Goodwin et al., 2002; Tassis, 2007), with mean axis ratios $b/a \approx 0.9$ and $c/a \approx 0.4 - 0.5$. Since the direction of the smallest axis (c) corresponds to our preferred direction of flattening (z), the deprojected b/a values can be compared directly with our models. We find reasonable agreement for the subcritical models 1 and 2. The deprojected values of c/a can also be compared with our thin-sheet models, in which effectively $c/a = \langle Z \rangle/a = \langle Z \rangle \sqrt{\langle b/a \rangle}/\langle s \rangle$. There is reasonable agreement here again for the subcritical models 1 and 2, as well as for the highly supercritical model 6, which have, respectively, $c/a = 0.49, 0.43,$ and 0.49.

3.2.5. *Core Mass Distributions*

In Fig. 8 we present histograms of core mass distributions generated from the multiple runs of models 1 through 6, as described in Section 3.2.4. Each core is defined as an
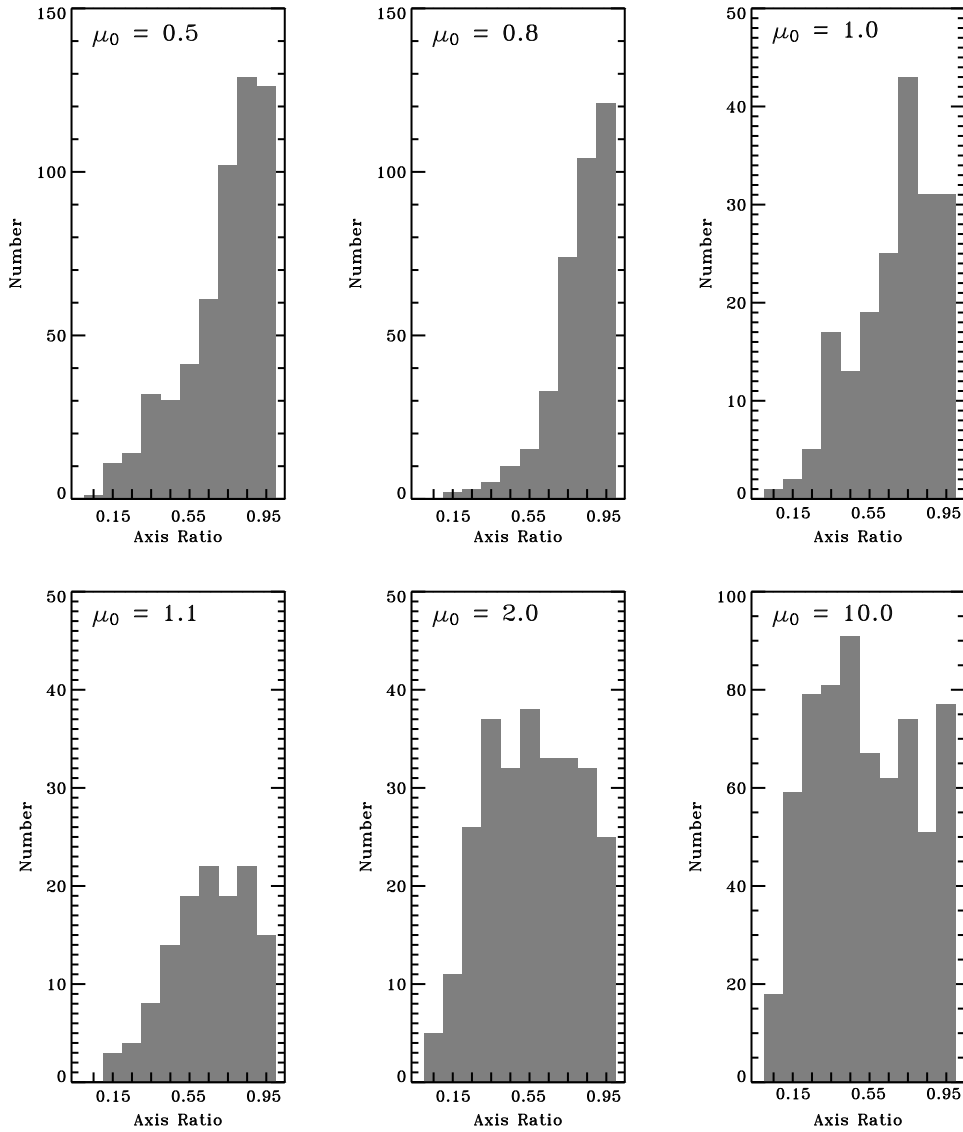
21

Fig. 7. Histograms of axis ratios b/a of best fit ellipses to dense regions with $\sigma_n/\sigma_{n,0} \geq 2$, measured at the end of simulations with $\mu_0 = 0.5, 0.8, 1.0.1.1, 2.0, 10.0$ as labeled, corresponding to models 1 through 6 in Table 2. Each figure is the result of a compilation of results of a large number of simulations. The bin width is 0.1.

enclosed region with $\sigma_n/\sigma_{n,0} \geq 2$ that is present at the end of the simulation, when $\sigma_{n,max}/\sigma_{n,0} = 10$. For comparison with observations, we have converted our calculated masses to $M_\odot$ using an assumed background number column density $N_{n,0} = 10^{22}$ cm^{-2} and temperature $T = 10$ K (see Eq. [24]).

We note that the variation of the peak masses (and the average masses tabulated in

22

Table 2) from one model to another are in qualitative agreement with the predictions of linear theory (Table 1). Furthermore, the $\mu_0 = 0.5$ and $\mu_0 = 10$ models generate very similar core mass distributions that are difficult to distinguish. This is not surprising since they have such similar preferred fragmentation scales.

The striking feature of each of the histograms is the very sharp descent at masses greater than the peak of the distribution. Gravitational fragmentation yields a very strong preferred mass scale. The peak value itself is more ambiguous and can vary according to the magnetic field strength, the background column density, the cloud temperature, and the contour level we use to define the core. In contrast, the slope on the low-mass side is much shallower. This is due to the capture of emerging cores at the end of any simulation. Many of those cores are expected to grow in time and move over to the right by the time their peaks undergo runaway collapse and form a star. The distribution may be described as relatively narrow and lognormal-like, but with a broader tail at the low-mass side due to the temporal spread of core ages.

The steep decline of the of the mass distributions beyond the peak ($d \log N / d \log M \approx -5$ is typical) in our study is in contrast to that observed for condensations in cluster forming regions (e.g. Motte et al., 1998), where $d \log N / d \log M \approx -1.5$ at high masses. Gravitational fragmentation under the conditions studied in this paper and at the time snapshot chosen here yields a very strong preference for a characteristic mass. We discuss possible mechanisms of broadening the mass distribution in Section 4.

3.2.6. *Supercritical Cores*

For clouds that start with subcritical or transcritical initial conditions, there is available a more physical definition of a "core", i.e. a region that is significantly supercritical and enclosed within a subcritical common cloud envelope. Axisymmetric simulations of cores that evolve initially by ambipolar drift have shown that the contraction becomes very rapid by the time that $\mu \approx 2$ in the central region, leaving behind a more slowly evolving and essentially subcritical envelope (see, e.g. Fiedler & Mouschovias, 1993; Ciolek & Mouschovias, 1994; Basu & Mouschovias, 1994).

Fig. 9 shows images and contour maps of $\mu(x, y)$ at the end of the simulation for models 1 and 3, respectively. The initially subcritical ($\mu_0 = 0.5$) model 1 has peaks in $\mu(x, y)$ coinciding with the major peaks in $\sigma(x, y)$ (see Fig. 3 upper left). However, note that the density condensations are either largely or even entirely subcritical ($\mu < 1$) at this stage. This image shows that subcritical clouds can have observable density enhancements which may still be partially or entirely subcritical, because they are still in the process of ambipolar-drift-driven gravitational instability. The image and contours for the initially critical ($\mu_0 = 1.0$) cloud shows that the cloud naturally separates into supercritical and subcritical regions, due to ambipolar diffusion and a fixed total magnetic flux threading the cloud. The newly created supercritical regions are extended and typically contain more than one density and mass-to-flux ratio peak within them. In this case, all density peaks are associated with gas that has $\mu > 1$.

The presence of supercritical regions embedded within a common subcritical envelope allows us to define cores in a more physical way than the previous definition as regions with $\sigma_n / \sigma_{n,0} \geq 2$. The latter is a somewhat arbitrary designation, as indeed are all observational definitions of cores. However, the definition of supercritical cores has its own ambiguities, as a simple definition of regions with $\mu > 1$ yields extended regions in
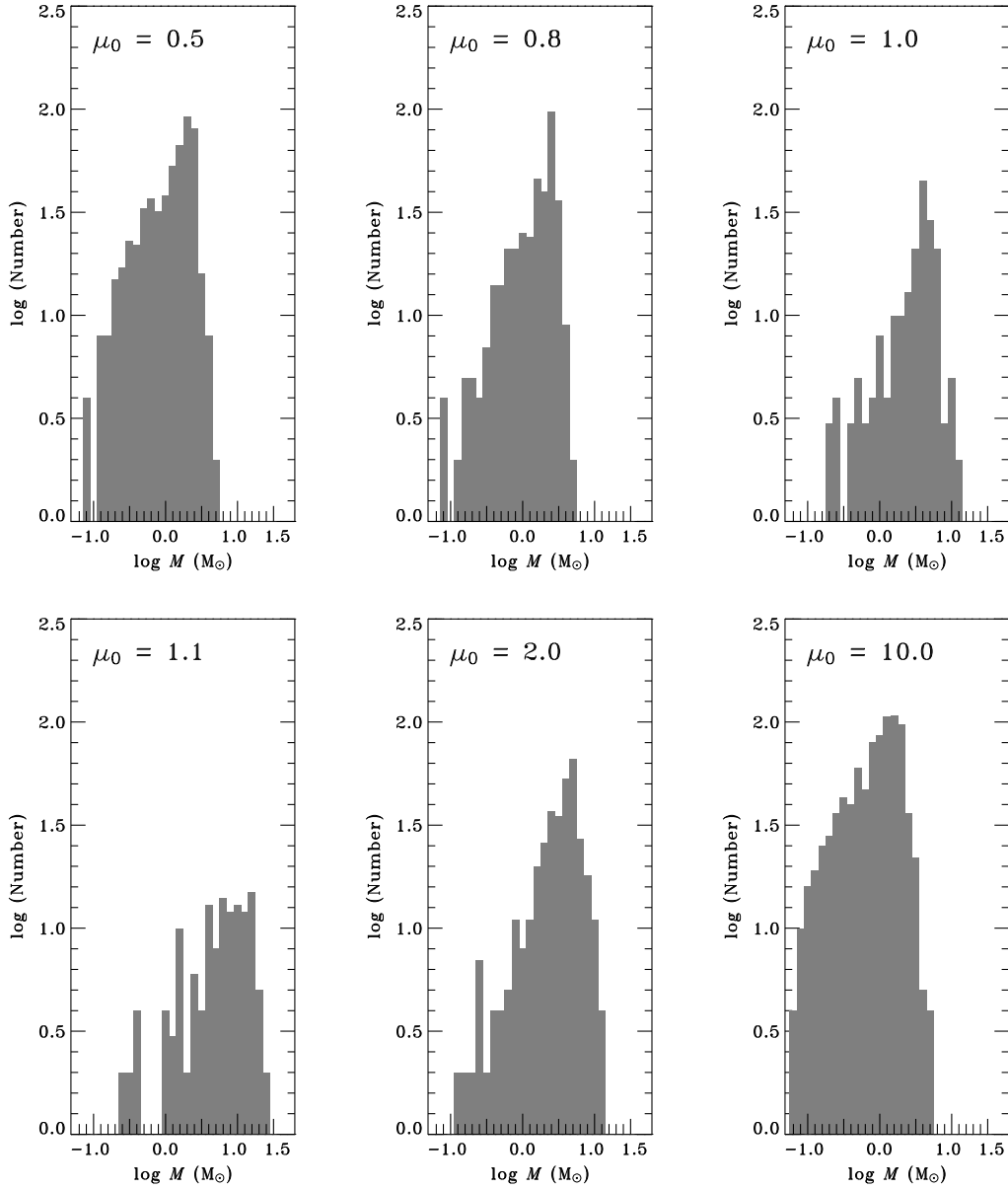
Fig. 8. Histograms of masses contained within regions with $\sigma_n/\sigma_{n,0} \geq 2$, measured at the end of simulations with $\mu_0 = 0.5, 0.8, 1.0.1.1, 2.0, 10.0$ as labeled. Each figure is the result of a compilation of results of a large number of simulations. The bin width is 0.1.

model 3 with multiple density peaks. We find that a viable working definition is that a core is a region with $\mu > 1.3$. This isolates individual density peaks in both models, and is consistent with the earlier axisymmetric findings that a mass-to-flux ratio somewhat *above* the critical value is necessary before rapid collapse and separation from the envelope becomes apparent. For example, Ciolek & Mouschovias (1993) found that $\mu > 1.23$ was

24
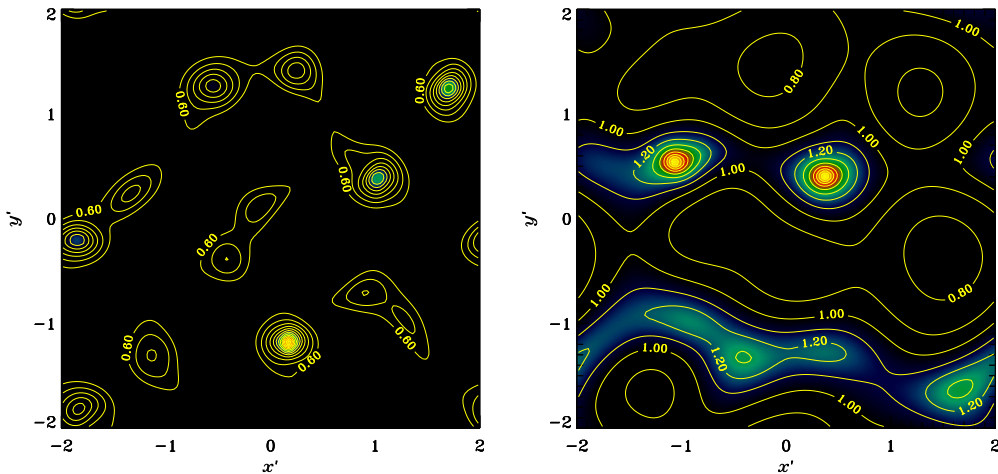
Fig. 9. Image and contours of $\mu(x, y)$, the mass-to-flux ratio in units of the critical value for collapse. Regions with $\mu > 1$ are displayed with a color table, while regions with $\mu < 1$ are black. The contour lines are spaced in additive increments of 0.1. Left: Final snapshot of simulation with $\mu_0 = 0.5$. Right: Final snapshot of simulation with $\mu_0 = 1.0$.

required for the absence of any available axisymmetric equilibrium state, using a similar value of $\tilde{P}_{\mathrm{ext}}$ as we do. We compile data from 100 runs of each model with distinct random realizations of the initial states and present the core mass distribution for each of models 1 and 3 in Fig. 10. The conversion to dimensional masses is done in the same manner as for Fig. 8. The resulting distributions have a peak mass that is somewhat smaller than found using the different core definition used for Fig. 8. However, these distributions also have a very sharp decline at higher masses.

3.3. The Effect of Varying $\tilde{\tau}_{\mathrm{ni},0}$

Eq. (27) shows that the ionization fraction x_{i} at a given neutral density n_{n} increases (decreases) linearly as $\tilde{\tau}_{\mathrm{ni},0}$ decreases (increases). We investigate the effect of decreasing and increasing $\tilde{\tau}_{\mathrm{ni},0}$ by a factor of two from its standard value (which can be accomplished by changing the factor $\mathcal{K}$ in Eq. [18]) in models 7 and 8, respectively. The other two parameters are kept fixed at $\mu_0 = 1.0$ and $\tilde{P}_{\mathrm{ext}} = 0.1$. The characteristic growth times of instability $\tau_{\mathrm{g,m}}$ scale approximately $\propto \tilde{\tau}_{\mathrm{ni},0}^{-1} \propto x_{\mathrm{i},0}$ (see also Table 1), where $x_{\mathrm{i},0}$ is the ionization fraction at the background number density $n_{\mathrm{n},0}$. Models 7, 3, and 8 have $\tilde{\tau}_{\mathrm{ni},0} = (0.1, 0.2, 0.4)$, $\tau_{\mathrm{g,m}} = (27.5, 14.3, 7.9) \times t_0$, and $\lambda_{\mathrm{g,m}} = (28.5, 24.3, 20.0) \times L_0$, respectively. Furthermore, Table 2 reveals that the time to runaway collapse ($\sigma_{\mathrm{n,max}}/\sigma_{\mathrm{n},0} \geq 10$) is $\approx 10\,\tau_{\mathrm{g,m}}$ when starting from small-amplitude white noise perturbations, as generally found in our parameter study. This means that our high ionization-fraction model 7 has the largest value of $t_{\mathrm{run}}(= 261\,t_0)$ in our parameter study. This also leads to the largest age spread of cores in any of our simulations. This is measured by the fact that a typical simulation, when run (for compiling statistics) in a large box with $L = 64\,\pi, N = 512$, has many cores that are just beginning to emerge when the first core goes into a runaway collapse. Hence, our value for $\langle \lambda \rangle$ is calculated with a lower core threshold $\sigma_{\mathrm{n}}/\sigma_{\mathrm{n},0} \geq \sqrt{2}$
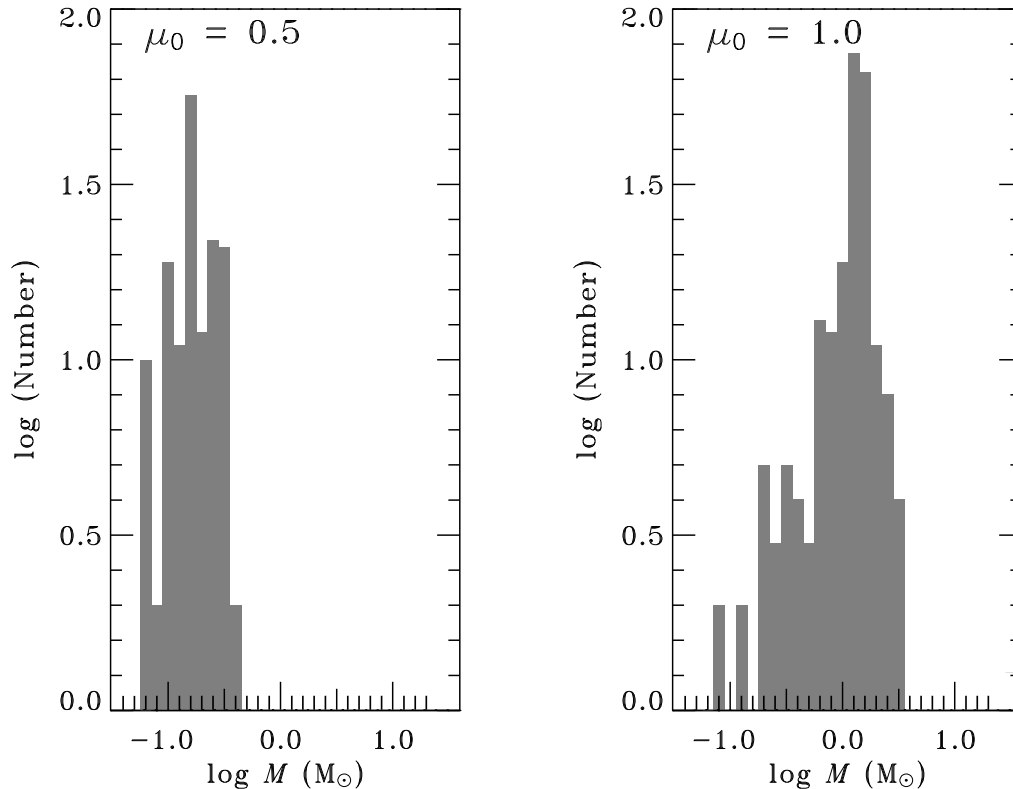
25

Fig. 10. Histogram of masses contained within regions that are significantly supercritical, specifically $\mu > 1.3$, measured at the end of simulations with $\mu_0 = 0.5$ and $\mu_0 = 1.0$. Each figure is the result of a compilation of results of a large number of simulations. The bin width is 0.1.

for this one model. Our analysis reveals that the fragmentation scales in the nonlinear phase are indeed comparable amongst models 3, 7, and 8, and in good agreement with the linear theory prediction. We conclude that the effect of varying ionization (for a fixed μ_0) within the range studied is primarily in the *rate* of evolution.

Fig. 11 shows images and contours of the density, as well as velocity vectors, for models 7 and 8. The time to reach runaway collapse is about four times longer for model 7 than for model 8, consistent with its value of $\tilde{\tau}_{\mathrm{ni},0}$ being four times smaller. Model 8 has $\tilde{\tau}_{\mathrm{ni},0} = 0.4$, hence poorer neutral-ion coupling and therefore reduced magnetic support. This results in slightly greater infall speeds, slightly larger number of fragments, and cores which are slightly more elongated. These are all consistent with its more dynamical evolution.

3.4. *The Effect of Varying* $\tilde{P}_{\mathrm{ext}}$

Our models with $\tilde{P}_{\mathrm{ext}} = 10$ may represent the effect of pressured environments such as sheets brought together by the presence of shocked gas (e.g. stellar winds or supernovae) and being embedded in or adjoining an H II region. These models could represent an
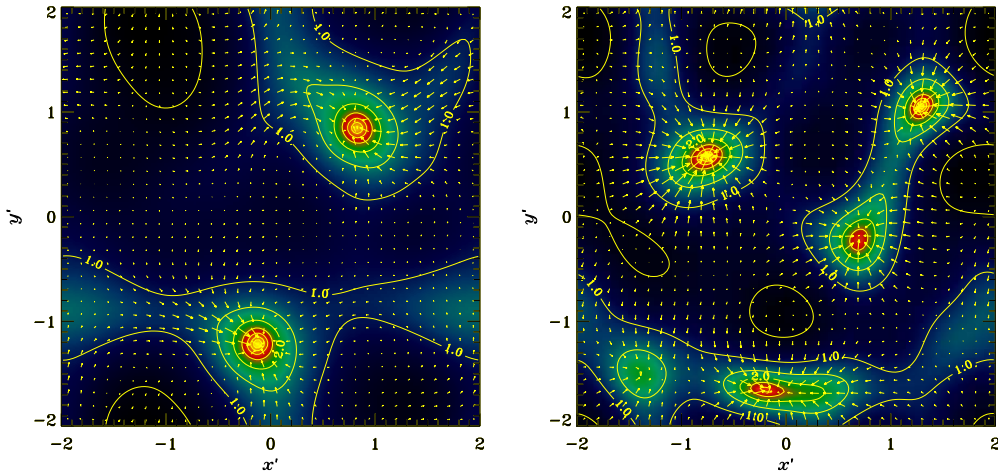
26

Fig. 11. Column density and velocity vectors as in Fig. 3, but for models with $\tilde{\tau}_{\mathrm{ni},0} = 0.1$ (left) and $\tilde{\tau}_{\mathrm{ni},0} = 0.4$ (right). Both models have $\mu_0 = 1.0$ and $\tilde{P}_{\mathrm{ext}} = 0.1$.

example of "induced" star formation in a manner related but not equivalent to that of an initial turbulent flow with high ram pressure.

Models 9 and 10 both develop extreme clustering in comparison to the other models. Table 2 shows that the fragmentation scales are about 1/3 to 1/4 of that for the corresponding models with the same mass-to-flux ratio but small $\tilde{P}_{\mathrm{ext}}$. The fragments grow initially through a pressure-driven mode and the spacing is in excellent agreement with the predictions of linear theory (Fig. 1 and Table 1). However, our results show that the nonlinear instability does develop into a gravitationally-driven runaway collapse. The maximum speeds are still subsonic at the end of our simulation, due to the relatively weak gravitational influence of each compact core. As well as having the smallest fragmentation scales, these models also have the shortest time scales to runaway collapse. For the fiducial $N_{\mathrm{n},0} = 10^{22}$ cm^{-2}, models 9 ($\mu_0 = 0.5$) and 10 ($\mu_0 = 1.0$) have values of $t_{\mathrm{run}} = (1.6 \text{ Myr}, 0.81 \text{ Myr})$ and $\langle \lambda \rangle = (5800 \text{ AU}, 7700 \text{ AU})$, respectively. Both sets of numbers are considerably smaller than for the models 1 and 3, which have corresponding values of μ_0 but $\tilde{P}_{\mathrm{ext}} = 0.1$. Fig. 12 shows the clustering properties of model 10 at the end of the simulation, which is very similar to the corresponding image for model 9 (not shown). This fragmentation model clearly produces a much richer cluster than in the relatively unpressured environments presented earlier. Velocity vectors are not shown in this image due to confusion arising from infall onto so many peaks. A careful inspection of the image reveals a variety of core spacings and sizes at this stage of evolution. Interestingly, the average core spacing $\langle \lambda \rangle = 5.3 L_0$ is in very good agreement with the preferred wavelength in linear theory, $\lambda_{\mathrm{g,m}} = 5.0 L_0$. These length scales are well resolved in our simulations. However, the average core mass $\langle M \rangle$ significantly exceeds the linear theory value $M_{\mathrm{g,m}}$. Only models 9 and 10 show such a large discrepancy between these values. We attribute it to the very small sizes of the cores (see $\langle s \rangle$ values in Table 2) in these simulations. This means that the cores themselves are barely resolved and the mass estimates should be taken as approximate values that likely represent upper limits.
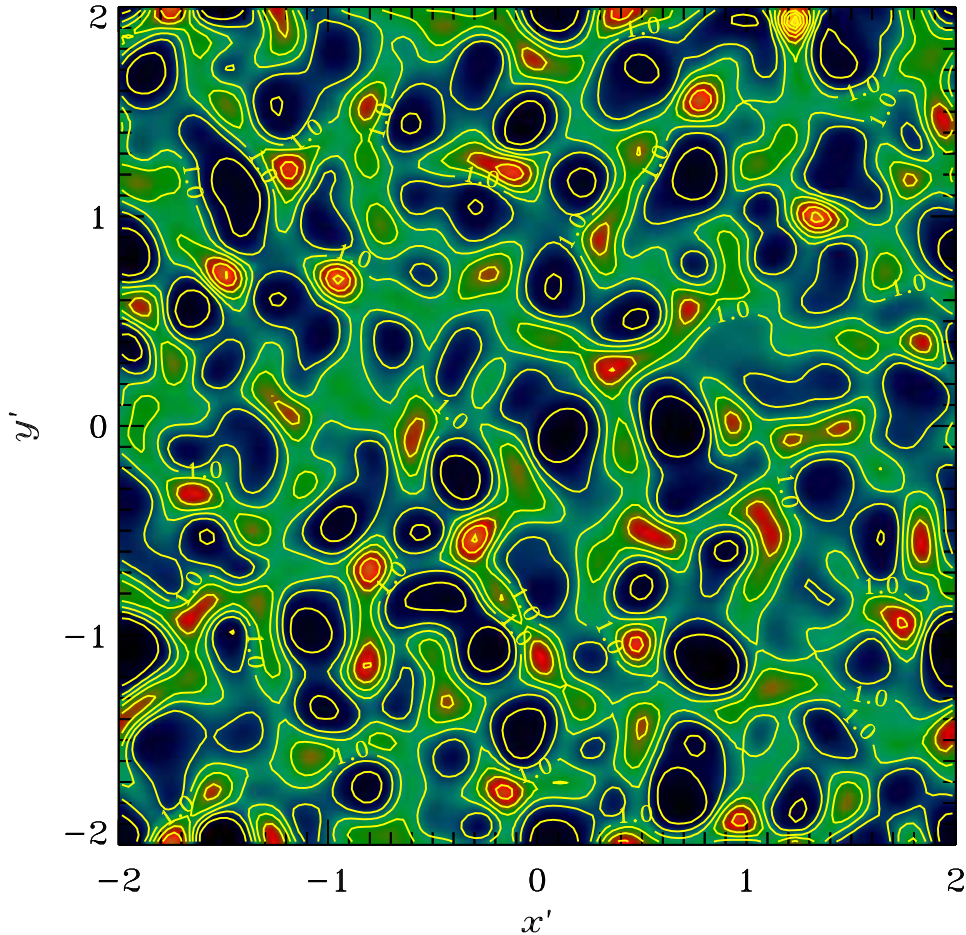
27

Fig. 12. Column density as in Fig. 3, but for a model with $\tilde{P}_{\mathrm{ext}} = 10$. Other parameters of this model are $\mu_0 = 1.0$ and $\tilde{\tau}_{\mathrm{ni},0} = 0.2$.

4. Discussion

Our simulations of the nonlinear development of gravitational instability under the influence of magnetic fields and ambipolar diffusion start from a background state of uniform column density and magnetic field strength. Small-amplitude white-noise perturbations initiate the evolution and eventually lead to the nonlinear growth of fragments. Averaging over a large number of simulations reveals that the average spacing of nonlinearly developed cores is essentially that predicted from the preferred fragmentation scales in linear perturbation theory (CB06). However, the time to reach fully developed runaway collapse is up to ten times longer than that of the eigenmode with minimum growth time $\tau_{\mathrm{g,m}}$. The quantity $\tau_{\mathrm{g,m}}$ itself varies from $\approx Z_0/c_{\mathrm{s}}$ (essentially the free-fall time $\approx 1/\sqrt{G\rho_{\mathrm{n},0}}$ for unpressured sheets) for highly supercritical models to $\approx 10Z_0/c_{\mathrm{s}}$ for highly subcritical models (for a typical neutral-ion coupling level). The times to reach

28

runaway collapse vary widely amongst models with different mass-to-flux ratios, ionization fractions, and external pressures. For a cloud with $N_{n,0} = 10^{22}$ cm^{-2} and $T = 10$ K, the times to reach runaway growth of the first core ranges from 0.45 Myr to 9.53 Myr (see Table 2). Since our simulations start from a flat density background, these times represent *upper limits* to the time that fragmentation might take for each set of parameters. However, an advantage of the uniform background density is that it allows for a self-consistent modeling of the entire core formation process, without questions about the origin of initially peaked density distributions used in earlier axisymmetric calculations (e.g. Ciolek & Mouschovias, 1993; Basu & Mouschovias, 1994).

In a medium with initial nonlinear perturbations, the time scales for all sets of parameters are indeed likely to be shorter. However, we believe that our calculated time scales are relevant if the corresponding dimensional values are obtained from higher starting values of column density brought about in certain regions by pre-existing (including turbulent) flows. For example, the Taurus molecular cloud has an overall background number column density $N \approx (1-2) \times 10^{21}$ cm^{-2} but also contains embedded dark clouds with $N \approx 5 \times 10^{21}$ cm^{-2}, such as HCl 2 and L1495, within which there are small clusters of $\sim 10-20$ YSO's and also many dense cores (see Gomez et al., 1993; Onishi et al., 2002; Goldsmith et al., 2008). Our periodic model may be applied to such dark clouds that may themselves have been brought together by nonlinear flows originating in the larger cloud, external triggers, or an earlier phase of gravitational fragmentation. A second example application of our periodic model may be within the L1688 dark cloud in Ophiuchus, which has $N \approx 10^{22}$ cm^{-2} (Motte et al., 1998). The mean spacing of fragments in these two regions varies (André et al., 2000), with core edges measured to be at radii $\lesssim 5000$ AU in L1688 but at $\lesssim 20000$ AU in the Taurus dark clouds (André et al., 2000). While some of the difference in spacing may be due to the different background column densities, other important aspects of spatial and kinematic structure may also arise due to different values of μ_0 and $\tilde{P}_{\text{ext}}$ (and $\tilde{\tau}_{\text{ni},0}$ to a lesser extent), as demonstrated in this paper.

Unlike a uniform density three-dimensional medium, our thin sheet actually has a preferred scale for gravitational fragmentation with a unique value for any given set of initial dimensionless parameters. Since our simulation region is always safely larger than this fragmentation scale, it is unlikely that the size of our system (in the x- and y-directions) influences the final outcome, as measured by fragment spacings, time scales to runaway collapse, and core mass distributions, for example. This is supported by our tests with runs at quadruple the size of the standard simulations. Incidentally, this is not the case for three-dimensional periodic box simulations, in which the fastest growing mode of gravitational instability is always that of the box size. We believe that a stratified medium is also a more physical and realistic starting point than a uniform three-dimensional medium. This is because the formation process of molecular clouds, or magnetic fields and nonlinear flows within it, will tend to set up compressed regions with a characteristic scale similar to the half-thickness $Z_0 \approx c_s^2/(\pi G \sigma_{n,0})$ of our adopted background reference sheet geometry. That scale is related to the Jeans scale and effectively determines the preferred fragmentation scale, as modified by magnetic field strength, ionization fraction, and external pressure.

The core mass distributions that we have compiled from our simulations are narrowly-peaked and do not match the broader distributions commonly observed in cluster-forming regions (e.g. Motte et al., 1998). What is the missing physics that can explain the discrep-
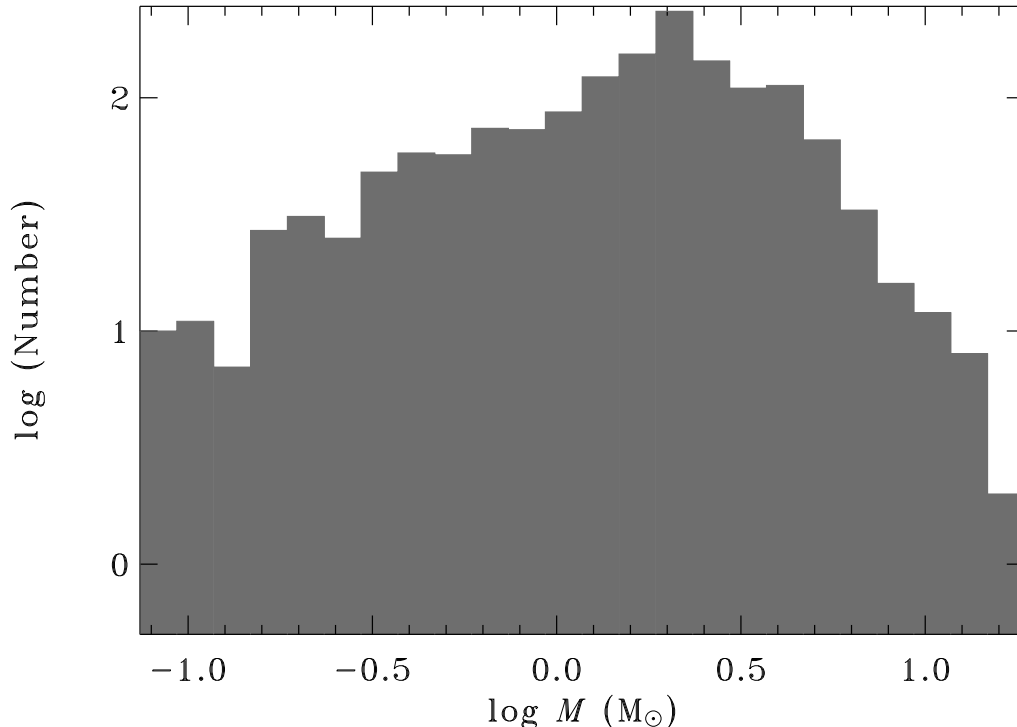
29

Fig. 13. Histogram of masses from models with $\mu_0 = 0.5, 0.8.1.0, 1.1, 2.0$ and $\tilde{\tau}_{\mathrm{ni},0} = 0.2, \tilde{P}_{\mathrm{ext}} = 0.1$. A weighted average of core masses is taken, so that an equal simulated area is assigned to each of models $1 - 5$. The cores are the same as the ones in the first five panels of Fig. 8. The bin width is 0.1.

ancy? The explanation that is closest to the spirit of our models is that real molecular clouds start their lives with an inhomogeneous distribution of physical quantities, including the mass-to-flux ratio. We expect that the values of μ in a molecular cloud may fall within the observationally-established range of $[0.5, 2]$, i.e. within a factor of two of the critical value in each direction. In that case, we can make a simple estimate of a core mass distribution by adding up the histograms for the five models with $\mu_0 = [0.5, 0.8.1.0, 1.1, 2.0]$ shown in Fig. 8. Since the model with $\mu_0 = 1.1$ is run fewer times but with a larger box size, we sample the number of cores necessary to give equal area weighting with the other models. The resulting histogram is presented in Fig. 13. The broad variation of peaks in the individual histograms seen in Fig. 8 leads to a smooth power-law tail in the high mass end of the composite histogram. Fig. 13 reveals a slope $d \log N/d \log M \approx -2$ in this region, only somewhat steeper than the value $d \log N/d \log M \approx -1.5$ measured for example by Motte et al. (1998). We note that this general mechanism, arising from an initially inhomogeneous distribution of mass-to-flux ratio, is an interesting new possibility for explaining the observed broad core mass distributions. An important point is that a relatively *narrow* distribution of initial mass-to-flux ratios (factor of a few variation) can lead to a relatively broad distribution of fragment masses. This mechanism remains to be explored more generally and does not exclude the occurrence of other mechanisms like competitive accretion in a more global model (Bonnell et al., 2003), a temporal spread of core accretion lifetimes (Myers, 2000; Basu

& Jones, 2004), and turbulent fragmentation (e.g. Padoan et al., 1997; Klessen, 2001; Gammie et al., 2003; Tilley & Pudritz, 2007).

The richness of the physics revealed by our models of gravitational fragmentation up to runaway collapse of the first core, under conditions of varying mass-to-flux ratio, ionization level, and external pressure, pave the way for more extensive models in the future. Adding the effects of initial cloud turbulence, implementing a technique for integrating past the formation of the first generation of stars, and including some form of energy feedback from star formation, remain to be done. The addition of new and more complex effects will be facilitated by the fact that the thin-sheet approximation allows efficient calculation of the fragmentation process while retaining a high level of realism. In this context we point out that the recent fully three-dimensional fragmentation simulation of Kudoh et al. (2007) with magnetic fields and ambipolar diffusion bears out the main physical results presented by BC04.

5. Summary

We have carried out a large number of model simulations to study the effect of initial mass-to-flux ratio, neutral-ion coupling, and external pressure on dense core formation from gravitational fragmentation of isothermal sheet-like layers that may be embedded within larger molecular cloud envelopes. Our simulation box is periodic in the lateral (x, y) directions and typically span four nonmagnetic (Jeans) fragmentation scales in each of these directions. The simulations reveal a wide range of outcomes, from the unique transcritical fragmentation mode into massive cores, to the pressure-driven fragmentation into dense clusters. We emphasize the following main results of the paper:

(i) *Fragmentation Spacing.* The average spacings of nonlinearly developed fragments are generally in excellent agreement with the preferred fragmentation scale of linear perturbation theory (Ciolek & Basu, 2006), although there is definite irregularity in any simulation, with variation of fragment spacings. Both significantly subcritical *and* highly supercritical clouds have average fragmentation scales $\langle \lambda \rangle \approx 2\pi Z_0$, where Z_0 is the half-thickness of the background state. The transcritical ($\mu_0 \approx 1$) models exhibit very large (super-Jeans) average fragment spacings, although there is evidence for nonlinear second-stage fragmentation in some cases, which makes the average spacing slightly smaller than predicted by linear theory. Variation of the ionization fraction by a factor of two above and below the standard value does not have a big effect on fragment spacing. However, an external pressure dominated sheet undergoes dramatically smaller scale fragmentation to form a dense cluster.

(ii) *Time Evolution to Runaway.* The times t_{run} for various models to reach runaway collapse of the first core varies significantly for models with differing initial dimensionless mass-to-flux ratio μ_0, neutral-ion coupling parameter $\tilde{\tau}_{\mathrm{ni},0}$, and dimensionless external pressure $\tilde{P}_{\mathrm{ext}}$. Values of t_{run} range from 0.45 Myr to 9.53 Myr, each scaling as $(N_{\mathrm{n},0}/10^{22} \ \mathrm{cm}^{-2})^{-1}(T/10 \ \mathrm{K})^{1/2}$. The supercritical clouds evolve much more rapidly than the critical or subcritical clouds, with the highly supercritical clouds evolving ≈ 10 times more rapidly than a critical cloud, for the typical level of neutral-ion coupling. A critical cloud in turn evolves more rapidly than a subcritical cloud, but the variation is a factor of order unity for plausible initial values of μ_0; for example the $\mu_0 = 0.5$ model reaches runaway collapse in a time that is 1.7

31

times longer than for the $\mu_0 = 1$ model. In all cases, the time to runaway collapse is $\approx 10\,\tau_{\mathrm{g,m}}$ when starting with small-amplitude white noise perturbations, where $\tau_{\mathrm{g,m}}$ is the growth time of the fastest growing eigenmode mode in linear perturbation theory. The quantity $\tau_{\mathrm{g,m}}$ itself varies from $\approx Z_0/c_{\mathrm{s}}$ for highly supercritical models to $\approx 10 Z_0/c_{\mathrm{s}}$ for highly subcritical models (for a typical neutral-ion coupling level). The effect of varying $\tilde{\tau}_{\mathrm{ni,0}}$ (and hence the initial ionization fraction $x_{\mathrm{i,0}}$) is that $t_{\mathrm{run}} \propto \tilde{\tau}_{\mathrm{ni,0}}^{-1} \propto x_{\mathrm{i,0}}$ approximately for ambipolar-drift-driven (critical or subcritical) fragmentation, so that the canonical $\tau_{\mathrm{g,m}} \approx 10 Z_0/c_{\mathrm{s}}$ and our calculated $t_{\mathrm{run}} \approx 100 Z_0/c_{\mathrm{s}}$ are both possibly subject to significant variation. A pressure dominated cloud with $\tilde{P}_{\mathrm{ext}} = 10$ has t_{run} about 5-6 times shorter than clouds with small external pressure but other parameters held fixed.

(iii) *Velocities in the Nonlinear Regime.* Maximum infall speeds of neutrals can become supersonic on core scales in the supercritical clouds, but remain subsonic for critical or subcritical clouds. The latter is true even if the ionization fraction is reduced by a factor of two. The ion speeds in the cores closely follow the neutral speeds but are somewhat smaller, since the gravitationally-driven motion of the neutrals is generally opposed in the plane of the sheet by magnetic fields.

(iv) *Core Shapes.* An extensive compilation of core shapes shows that the distributions have a peak that is near-circular for the subcritical and critical fragmentation models. However, the cores become more elongated in the sheet for supercritical clouds, with a mean axis ratio in the sheet plane ≈ 0.5. The half-thickness remains smaller than either semiminor or semimajor axis in the sheet, so that the cores are triaxial and preferentially flattened along the direction of the mean magnetic field. Preliminary comparison of our results with published deprojections of the observed axis ratios of cores shows the best agreement with our subcritical models.

(v) *Core Mass Distributions.* An extensive compilation of core masses shows that the peak of the distributions are related to the preferred fragmentation mass $M_{\mathrm{g,m}}$ of linear theory. Transcritical fragmentation yields the largest peak masses while the highly supercritical and decidely subcritical limits have smaller (Jeans-like) peaks and similar distributions. That the peak mass is strongly selected is seen in the very sharp drops in the distributions for greater masses. This means that the observed relatively broad-tailed core mass distributions cannot be explained by a pure local gravitational fragmentation process in a medium of uniform background column density and mass-to-flux ratio. Cores defined as significantly supercritical regions within a larger subcritical common envelope also have a very narrowly-peaked distribution. However, a composite mass histogram that may mimic the effect of an inhomogeneous assortment of initial mass-to-flux ratios, does produce a broad core mass distribution that resembles its observed counterparts.

(vi) *Magnetic Field Line Structure.* Contraction of cores within a supercritical cloud yields significant curvature of the magnetic field lines and very apparent hourglass morphologies, since contraction proceeds primarily with field-line dragging. The transcritical and subcritical clouds form cores through a process driven in large part by neutral-ion slip, and result in lesser curvature in the magnetic field. This holds out the hope of using the observed curvature of possible future observations of hourglass magnetic fields on the core scale as a proxy for measuring the ambient mass-to-flux ratio.

Acknowledgements

References

Alves, F. O., Franco, G. A. P. 2007. A&A 470, 597.

André, P., Ward-Thompson, D., Motte, F. 1996. A&A 314, 625.

André, P., Ward-Thompson, D., Barsony, M., 2000. In: Mannings, V., Boss, A. P., Russell S. S. (Eds.), Protostars and Planets IV. University of Arizona Press, Tucson, p. 59.

Bacmann, A., André, P., Puget, J.-L., Abergel, A., Bontemps, S., Ward-Thompson, D. 2000. A&A 361, 555.

Basu, S., Ciolek, G. E. 2004. ApJ 607, L39 (BC04).

Basu, S., Jones, C. E. 2004. MNRAS 347, L47.

Basu, S., Mouschovias, T. Ch. 1994. ApJ 432, 720.

Bate, M. R., Bonnell, I. A., Bromm, V. 2003. MNRAS 339, 577.

Benson, P. J., Myers, P. C. 1989. ApJS 71, 89.

Bonnell, I. A., Bate, M. R., Vine, S. G. 2003. MNRAS 343, 413.

Bourke, T. L., Myers, P. C., Robinson, G., Hyland, A. R. 2001. ApJ 554, 916.

Caselli, P., Walmsley, C. M., Zucconi, A., Tafalla, M., Dore, L., Myers, P. C. 2002. ApJ 565, 331.

Ciolek, G. E. 1996. In: Roberge, W. G., Whittet, D. C. B. (Eds.), Polarimetry of the Interstellar Medium. ASP Conference Series Vol. 97. Astronomical Society of the Pacific, p. 542.

Ciolek, G. E., Basu, S. 2006. ApJ 652, 442 (CB06).

Ciolek, G. E., Mouschovias, T. Ch. 1993. ApJ 418, 774.

———. 1994. ApJ 425, 142.

———. 1998. ApJ 504, 280.

Cortes, P. C., Crutcher, R. M., Watson, W. D. 2005. ApJ 628, 780.

Crutcher, R. M. 1999. ApJ 520, 706.

Crutcher, R. M., Nutter, D. J., Ward-Thompson, D., Kirk, J. M. 2004. ApJ 600, 279.

Elmegreen, B. G. 1979. ApJ 232, 729.

———. 2007. ApJ 668, 1064.

Elmegreen, B. G., Elmegreen, D. M. 1978. ApJ 220, 1051.

Elmegreen, B. G., Falgarone, E. 1996. ApJ 471, 816.

Fatuzzo, M., Adams, F. C. 2002. ApJ 570, 210.

Fiedler, R. A., Mouschovias, T. Ch. 1993. ApJ 415, 680.

Folini, D., Heyvaerts, J., Waleder, R. 2004. A&A 414, 559.

Fuller, G. A., Myers, P. C. 1993. ApJ 418, 273.

Gammie, C. F., Lin, Y.-T., Stone, J. M., Ostriker, E. C. 2003. ApJ 592, 203.

Goldsmith, P. F., Heyer, M., Narayanan, G., Snell, R., Li, D., Brunt, C. 2008. ApJ 680, 428.

Gomez, M., Hartmann, L., Kenyon, S. J., Hewett, R. 1993. AJ 105, 1927.

Goodman, A. A., Bastien, P., Myers, P. C., Ménard, F. 1990. ApJ 359, 363.

Goodman, A. A., Barranco, J. A., Wilner, D. J., Heyer, M. H. 1998. ApJ 504, 223.

Goodwin, S. P., Ward-Thompson, D., Whitworth, A. P. 2002. MNRAS 330, 769.

Heitsch, F., Hartmann, L. W., Slyz, A. D., Devriendt, J. E. G., Burkert, A. 2008. ApJ 674, 316.

Hennebelle, P., Banerjee, R., Vázquez-Semadeni, E., Klessen, R., Audit, E. 2008. A&A submitted (arXiv:0805.1366).

Heyer, M., Gong, H., Ostriker, E., Brunt, C. 2008. ApJ 680, 420.

Indebetouw, R., Zweibel, E. G. 2000. ApJ 532, 361.

Jeans, J. H. 1929. Astronomy and Cosmogony. Cambridge University Press, Cambridge.

Jijina, J., Myers, P. C., Adams, F. C. 1999. ApJS 125, 161.

Johnstone, D., Di Francesco, J., Kirk, H. 2004. ApJ 611, L45.

Jones, C. E., Basu, S. 2002. ApJ 569, 280.

Jones, C. E., Basu, S., Dubinski, J. 2001. ApJ 551, 387.

Kim, W.-T., Ostriker, E. C., Stone, J. M. 2002. ApJ 581, 1080.

Kirk, J. M., Ward-Thompson, D., André, P. 2005. MNRAS 350, 1506.

Klessen, R. S. 2001. ApJ 556, 837.

Kudoh, T., Basu, S. 2003. ApJ 595, 842.

———. 2006. ApJ 642, 270.

Kudoh, T., Basu, S., Ogata, Y., Yabe, T. 2007. MNRAS 380, 499.

Lada, C. J., Lada, E. A. 2003. ARAA 41, 57.

Lada, C. J., Alves, J. F., Lombardi, M. 2007. In: Reipurth, B., Jewitt, D., Keil, K. (Eds.), Protostars and Planets V. University of Arizona Press, Tucson, p. 3.

Langer, W. D. 1978. ApJ 225, 95.

Larson, R. B. 1985. MNRAS 214, 379.

———. 2003. Rep. Prog. Phys. 66, 1651.

Lee, C. W., Myers, P. C., Tafalla, M. 2001. ApJS 136, 603.

Li, Z.-Y., Nakamura, F. 2004. ApJ 609, L83.

Lubow, S. H., Pringle, J. E. 1993. MNRAS 263, 701.

McDaniel, E. W., Mason, E. A. 1973. The Mobility and Diffusion of Ions and Gases. Wiley, New York.

McKee, C. F. 1989. ApJ 345, 782.

———. 1999. In: Lada, C. J., Kylafis, N. (Eds.), The Origin of Stars and Planetary Systems. Kluwer, Dordrecht, p. 29.

Mac Low, M.-M., Klessen, R. S. 2004. Rev. Mod. Phys. 76, 125.

Mestel, L., Spitzer, L. Jr. 1956. MNRAS 116, 503.

Miyama, S, Narita, S., Hayashi, C. 1987. Prog. Theor. Phys. 78, 1051.

Miyama, S, Narita, S., Hayashi, C. 1987. Prog. Theor. Phys. 78, 1273.

Motte, F., André, P., Neri, R. 1998. A&A 336, 150.

Mouschovias, T. Ch. 1978. In: Gehrels , T. (Ed.), Protostars and Planets. University of Arizona Press, Tucson, p. 209.

Muench, A. A., Lada, C. J., Rathborne, J. M., Alves, J. F., Lombardi, M. 2007. ApJ 671, 1820.

Myers, P. C. 1983. ApJ 270, 105.

———. 2000. ApJ 530, L119.

Myers, P. C., Benson, P. J. 1983. ApJ 266, 309.

Myers, P. C., Fuller, G. A., Goodman, A. A., Benson, P. J. 1991. ApJ 376, 561.

Nakamura, F., Li, Z.-Y. 2005. ApJ 631, 411.

———. 2008. ApJ submitted (arXiv:0804.4201).

Onishi, T., Mizuno, A., Kawamura, A., Tachihara, K., Fukui, Y. 2002. ApJ 575, 950.

Padoan, P., Nordlund, A., Jones, B. J. T. 1997. MNRAS 288, 145.

Parker, E. 1966. ApJ 145, 811.

Press, W. H., Teukolsky, S. A., Vetterling, W. T., Flannery, B. P. 1996. Numerical Recipes in Fortran 77: The Art of Scientific Computing (Vol. 1 of Fortran Numerical Recipes), 2nd. Ed. Cambridge, New York.

Price, D. J., Bate, M. R. 2008. MNRAS 385, 1820.

Schiesser, W. E. 1991. The Numerical Method of Lines: Method of Integration of Partial Differential Equations. Academic Press, San Diego.

Schleuning, D. A. 1998. ApJ 493, 811.

Shampine, L. F. 1994. Numerical Solution of Ordinary Differential Equations. Chapman & Hall, New York.

Shu, F. H., Adams, F. C., Lizano, S. 1987, ARA&A 25, 23.

Shu, F. H., Allen, A., Shang, H., Ostriker, E. C., Li, Z.-Y. 1999. In: Lada, C. J., Kylafis, N. (Eds.), The Origin of Stars and Planetary Systems. Kluwer, Dordrecht, p. 193.

Tafalla, M., Mardones, D., Myers, P. C., Caselli, P., Bachiller, R., Benson, P. J. 1998. ApJ 504, 900.

Tassis, K. 2007. MNRAS 379, L50.

Teixeira, P. S., Lada, C. J., Alves, J. 2005. ApJ 629, 276.

Tilley, D. A., & Pudritz, R. E. 2007. MNRAS 382, 73.

Umebayashi, T., Nakano, T. 1980. PASJ 32, 405.

van Leer, B. 1977. JCP 23, 276.

Vázquez-Semadeni, E., Ryu, D., Passot, T., González, R. F., Gazol, A. 2006. ApJ 643, 245.

Vázquez-Semadeni, E., Gómez, G. C., Jappsen, A. K., Ballesteros-Paredes, J., González, R. F., Klessen, R. S. 2007. ApJ 657, 870.

Ward-Thompson, D., Scott, P. F., Hills, R. E., André, P. 1994. MNRAS 268, 276.

Ward-Thompson, D., André, P., Crutcher, R., Johnston, D., Onishi, T., Wilson, C. 2007. In: Reipurth, B., Jewitt, D., Keil, K. (Eds.), Protostars and Planets V. University of Arizona Press, Tucson, p. 33.

Williams, J. P., Myers, P. C., Wilner, D. J., DiFrancesco, J. 1999. ApJ 513, L61.

Zweibel, E. G. 1998. ApJ 499, 746.

———. 2002. ApJ 567, 962.